



UNIVERSITÀ DI PARMA

ARCHIVIO DELLA RICERCA

University of Parma Research Repository

Astronomical tuning of the La Vedova section between 16.3 and 15.0 Ma. Implications for the origin of megabeds and the Langhian GSSP

This is a pre print version of the following article:

Original

Astronomical tuning of the La Vedova section between 16.3 and 15.0 Ma. Implications for the origin of megabeds and the Langhian GSSP / Turco, Elena; Hüsing, Silja; Hilgen, Frederik; Cascella, Antonio; Gennari, Rocco; Iaccarino, Silvia Maria; Sagnotti, Leonardo. - In: NEWSLETTERS ON STRATIGRAPHY. - ISSN 0078-0421. - 50:1(2017), pp. 1-29. [10.1127/nos/2016/0302]

Availability:

This version is available at: 11381/2824417 since: 2021-10-04T13:52:20Z

Publisher:

E. Schweizerbart'sche Verlagsbuchhandlung

Published

DOI:10.1127/nos/2016/0302

Terms of use:

Anyone can freely access the full text of works made available as "Open Access". Works made available

Publisher copyright

note finali coverpage

(Article begins on next page)

Parma, 29 November 2015

Dear Editors of Newsletters on Stratigraphy,

We hereby send you a manuscript entitled: *"Astronomical tuning of the La Vedova section between 15 and 16.3 Ma. Implications for the origin of megabeds and the Langhian GSSP"*, by Elena Turco, Silja Hüsing, Frederik Hilgen, Antonio Cascella, Rocco Gennari, Silvia Maria Iaccarino, Leonardo Sagnotti.

In this manuscript we present the astronomical tuning of the upper Burdigalian/lower Langhian succession exposed in the La Vedova section (Ancona, Italy). This succession, which encompasses the interval between 16.3 and 15 Ma and is one of the candidate sections for the formal definition of the Langhian Global Stratotype Section and Point (GSSP), represents the older extension of the La Vedova Beach section (Hüsing et al. 2010, *Earth and Planetary Science Letters* 290, 254–269).

In the present manuscript, we have revised the composite lithologic log and the high resolution integrated magnetostratigraphy and calcareous plankton biostratigraphy compared to an earlier publication (Turco et al. 2011, *Stratigraphy* 8, 89–110), as a result of the better exposure conditions of the succession. We present the original high-resolution magnetic susceptibility and elemental records and the astronomical tuning to eccentricity and precession/insolation of the succession. We thus obtained an astronomical time scale, and hence astronomical ages for calcareous plankton bio-events and magnetic reversals, for the younger part of the Middle Miocene Climatic Optimum (between 16.3 and 15.0 Ma) in the Mediterranean. Furthermore, we discuss the magnetobiostratigraphy and astronomical calibration of the section; we deal with uncertainties in the structure of the basic cycles, the phase relation and the astronomical solution, which can affect the astronomical tuning to precession; we discuss the climatic and/or tectonic control in the deposition of the succession and we provide evidences that the La Vedova section meets key requirements for the Langhian GSSP.

We would be grateful if you would consider this original paper for publication in your journal.

We suggest the names of four potential reviewers:

- Slah Boulila, CNRS - UMR 7193 IStEP 'Institut des Sciences de la Terre-Paris', Université Paris VI, France. E-mail address: slah.boulila@upmc.fr
- Katharina Billups, College of Earth, Ocean, and Environment, University of Delaware, USA. E-mail: kbillups@udel.edu
- Ann Holbourn – Institute of Geosciences, Marine Micropaleontology, Kiel (Germany). E-mail: ah@gpi.uni-kiel.de
- Mitchell Lyle, College of Earth, Ocean and Atmospheric Sciences, Oregon State University, USA e-mail address: mlyle@coas.oregonstate.edu

Yours sincerely

Elena Turco

1 **Astronomical tuning of the La Vedova section between 15 and 16.3 Ma. Implications for**
2 **the origin of megabeds and the Langhian GSSP.**

3

4 Elena Turco^{a*}, Silja Hüsing^b, Frederik Hilgen^c, Antonio Cascella^d, Rocco Gennari^a, Silvia Maria
5 Iaccarino^a, Leonardo Sagnotti^e

6

7 ^aDipartimento di Fisica e Scienze della Terra, Università di Parma, Parco Area delle Scienze 157/A, 43124
8 Parma, Italy

9 ^bPaleomagnetic Laboratory 'Fort Hoofddijk', Utrecht University, Budapestlaan 17, 3584 CD Utrecht, The
10 Netherlands

11 ^cDepartment of Earth Sciences, Utrecht University, Budapestlaan 4, 3584 CD Utrecht, The Netherlands

12 ^dIstituto Nazionale di Geofisica e Vulcanologia (INGV), Via della Faggiola 32, 56126 Pisa, Italy

13 ^eIstituto Nazionale di Geofisica e Vulcanologia (INGV), Via di Vigna Murata 605, 00143 Roma, Italy

14 * Corresponding author

15

16

17 **Abstract**

18 The Early-Middle Miocene, marked by the Middle Miocene Climatic Optimum (MMCO) followed
19 by the Middle Miocene Climate Transition (MMCT) towards cooler temperatures, represents a
20 crucial period in Earth's climate evolution. To understand this episode and reconstruct its origin and
21 the regional impact of the observed global changes, it is critical that high-resolution astronomical
22 age models are developed for climate sensitive regions around the world. One of these areas
23 undoubtedly is the Mediterranean, but so far no such an age model has been established for the
24 interval of the MMCO. Nevertheless, this interval is well exposed in the coastal cliffs along the
25 Adriatic Sea near Ancona (Italy), where it is characterized by the occurrence of 7 conspicuous
26 limestone beds, termed megabeds, alternated with marl intervals.

27 Here, we use the Lower La Vedova Beach section to construct an astronomical time scale for
28 the younger part of the MMCO in the Mediterranean. The tuning to ~100-kyr eccentricity seems
29 robust, but is less certain for precession in some intervals, as a consequence of uncertainties in the
30 phase relation and structure of the basic cycles, and in the astronomical solution. The tuning
31 nevertheless provides astronomical ages for calcareous plankton bio-events and magnetic reversals
32 for the interval between 15 and 16.3 Ma. Individual megabeds are related to the ~100-kyr
33 eccentricity cycle corresponding to eccentricity minima and the megabed interval itself is partly

34 controlled by the 405-kyr cycle, as it marks two successive minima and the maximum in between.
35 However, no relation with very long period eccentricity cycles is evident, and a link to a major
36 orogenic phase at the base of the Langhian and the likely associated Langhian transgression seems
37 more plausible. The higher sedimentation rate in the megabeds may be explained by the additional
38 preservation of biogenic silica, which may also explain the poor planktonic foraminiferal faunas.
39 With the integrated magnetobiostratigraphy and the tuning to eccentricity and to
40 precession/insolation, the Lower La Vedova Beach section meets key requirements for the Langhian
41 GSSP.

42

43 **Keywords:** Burdigalian/Langhian boundary, magnetobiostratigraphy, element geochemistry,
44 astronomical tuning, Mediterranean, environmental changes

45

46 **1. Introduction**

47 The Early-Middle Miocene represents a crucial period in Earth's climate evolution and is
48 characterized by the Middle Miocene Climatic Optimum (MMCO) between ~ 17 and ~ 15 Ma. This
49 climatic optimum is followed by a gradual decline in temperature during the Middle Miocene
50 Climate Transition (MMCT) between 15 and 14 Ma, culminating in the marked Mi3b oxygen isotope
51 shift at 13.8 Ma that supposedly reflects rapid growth of the East Antarctic Ice Sheet (Miller et al.
52 1991, Holbourn et al. 2005, 2013, 2014, Abels et al. 2005). In addition, the Middle Miocene is
53 portrayed by the Monterey carbon isotope excursion from ~ 17 till ~ 13.5 Ma (Vincent and Berger
54 1985, Woodruff and Savin 1991, Holbourn et al. 2007). To disentangle this intricate global climate
55 history, high-resolution tuned time scales are essential. For the Middle Miocene, such a time scale
56 is already available for the open ocean, with high-resolution benthic foraminifer isotope records
57 providing highly valuable insight in the pattern of global climate change during the Middle Miocene
58 (Holbourn et al. 2005, 2007, 2013, 2014, Tian et al. 2013).

59 To understand the origin and regional expression of the MMCO and MMCT, it is essential that
60 similar high-resolution time scales and proxy records are established for climate sensitive regions.
61 One of these areas undoubtedly is the Mediterranean, which is well known to record the impact of
62 both global and regional climate change and, in turn, may have influenced global climate change
63 through changes in gateway configuration affecting ocean circulation. Up to now, a tuned time
64 scale has been established for the MMCT in the Mediterranean (Hüsing et al. 2010, Mourik et al.
65 2010), showing that the deposition of the oldest dark organic-rich layers termed sapropels directly

66 postdate the Mi3b cooling event. However, a similar high-resolution time scale is lacking for the
67 MMCO. Integrated magnetobiostratigraphic records have recently been published from several
68 Mediterranean sections, including La Vedova in northern Italy (Turco et al. 2011a) and St. Peter's
69 Pool on Malta (Foresi et al. 2011), which are potentially suitable for astronomical tuning.

70 Here we will focus on the astronomical tuning to eccentricity and precession/insolation of the
71 La Vedova section of Turco et al. (2011a), which represents the downward extension of the La
72 Vedova Beach section of Hüsing et al. (2010). In this study we refer to this extension as the Lower
73 La Vedova Beach section to distinguish it from the (Upper) La Vedova Beach section of Hüsing et
74 al. (2010). The Lower La Vedova Beach section is marked by the occurrence of prominent
75 megabeds (Sandroni 1985, Montanari et al. 1997), which may represent the local expression of the
76 MMCO in the Mediterranean between 16.3 and 15 Ma. At the same time, it is presented as one of
77 the candidate sections for the formal definition of the Langhian Global Stratotype Section and Point
78 (GSSP) (Turco et al. 2011a, Iaccarino et al. 2011).

79

80 **2. Geological setting and section**

81 The Lower La Vedova Beach section is exposed along the coastal cliffs 3 km southeast of
82 Ancona (Italy) (Fig.1) and can be reached via steep paths going down the cliffs from La Vedova
83 village or by boat. The section represents the downward extension of the Upper La Vedova Beach
84 and La Vedova High Cliff sections of Hüsing et al. (2010) and Mourik et al. (2010), respectively,
85 dated astronomically between ~15 and 13.5 Ma. The entire La Vedova section belongs to the lower
86 portion of the Schlier Formation, a (hemi)pelagic unit deposited in the eastern part of the Umbria-
87 Marche basin, which formed part of the external domain of the NE verging thrust belt of the
88 Apennine orogen (for more details see Montanari et al. 1997). In particular, the investigated
89 section belongs to the Massive Member of the Schlier Formation and includes the megabeds
90 described by Sandroni (1985) as "7 composite but apparently massive layers of hemipelagic
91 marls". According to Montanari et al. (1997), the top of this member coincides with the Aldo level,
92 an ash-bed that is located higher in the succession about 3 m above the top of our section in the
93 lower part of the Upper La Vedova Beach section of Hüsing et al. (2010).

94 **2.1. Revised composite section and magnetobiostratigraphy of the Lower La Vedova**

95 **Beach section**

96 The high-resolution integrated magnetostratigraphy and calcareous plankton biostratigraphy of
97 the section have recently been published (Turco et al. 2011a). However, much improved outcrop

98 conditions after severe winter storms during 2011 and 2012 (Fig. 2; Supplementary material A,
99 Figs. A1a-d) increased the accuracy of the lithologic description and revealed the presence of a
100 fault in the megabed interval in the lower part of the section. Determining the offset of this fault
101 was difficult in the field and, in addition, was beyond the resolution of the calcareous plankton
102 zonations and magnetostratigraphy as it falls within the planktonic foraminifer Subzone MMi4a, the
103 calcareous nannofossil Subzone MNN4b and Chron C5Br (Turco et al. 2011a). To check this offset,
104 extra samples for biostratigraphic analysis were taken from the better exposed left side of the
105 fault; the quantitative distribution pattern of selected calcareous plankton marker species
106 (*Globoturbotalita woodi*, *Globoquadrina dehiscens* and *Helicosphaera ampliapertura*) in the critical
107 interval on both sides of the fault indicates that one megabed is missing in the composite section of
108 Turco et al. (2011a) (Supplementary material A, Fig. A2). A comparison of the internal pattern of
109 the megabeds on both sides of the fault with the pattern observed in the cliffs just south of
110 Ancona, where the 7 megabeds are very well exposed in an undisturbed succession, suggests that
111 the missing megabed is Megabed VI according to the numbering introduced by Montanari et al.
112 (1997) (Supplementary material A, Fig. A3). This is confirmed in detail by an abundance peak of *G.*
113 *dehiscens* occurring close to the top of Megabed VI and the presence of two newly detected ash
114 layers above Megabed VI both at La Vedova and in the cliffs near Ancona (Supplementary material
115 A, Figs. A2 and A3). The detection of the extra megabed in the succession and extra sampling for
116 magnetostratigraphy and biostratigraphy resulted in a revised composite stratigraphic section and
117 magnetobiostratigraphic record, which compensates for the missing interval. These modified log
118 and magnetobiostratigraphic record are used as starting point for the present paper (Fig. 3). On
119 the basis of the updated magnetobiostratigraphic record, age calibrations of calcareous plankton
120 events have been recalculated and compared with those previously published by Turco et al.
121 (2011a) (Tab. 1).

122

123 **3. Material and methods**

124 **3.1. Lithology**

125 The lithologic log of Turco et al. (2011a) has been modified by taking the higher quality of the
126 exposures following the winter storms and the revised adjustment across the fault into account
127 (Figs. 2 and 3; Supplementary material A, Figs. A1, A2 and A3). The megabeds that are present in
128 the lower part of the section are numbered from I to VII following the codification of Sandroni
129 (1985) and Montanari et al. (1997). Above this interval we could recognize 6 additional indurated

130 intervals and decided to extend the numbering on the megabed scale to the top of the section, but
131 displaying the roman numerals (VIII-XIII) in italics to distinguish them from the real megabeds (I-
132 VII) in bold (Fig. 3). Next to the lithologic column, the fresh color of the small hand-drilled cores of
133 the samples is shown, which is based on the comparison of wet color of the cores with the Rock
134 Color Chart (Goddard et al. 1963). This comparison was previously described in Turco et al.
135 (2011a), who distinguished intercalations of greenish gray levels (5.0 GY 6/1), and more rarely
136 light olive gray (5.0 Y 5/2) and light bluish gray (5.0 B 7/1), within the predominant olive gray (5.0
137 Y 4/1) sediments.

138 **3.2. Planktonic foraminifera**

139 The planktonic foraminifer data set of Turco et al. (2011a) was enlarged by adding samples
140 from all the sediment color alternations present in the section in an attempt to find a relationship
141 between species abundance and lithology. In total 239 samples were analyzed applying the semi-
142 quantitative methodology described in Turco et al. (2011a), whereas 91 samples were studied only
143 qualitatively because of the very poor preservation (mainly in limestone layers) or the scarcity of
144 planktonic foraminifera (mainly in the megabeds).

145 **3.3. Geophysical proxy (MS)**

146 The magnetic susceptibility (MS) of 566 samples was measured on a Kappabridge KLY-2 and
147 their weight on a Sartorius RC 210 P. The specific magnetic susceptibility (m^3/kg) was calculated
148 by dividing the magnetic susceptibility of the sample by its weight.

149 **3.4. Geochemical elements (XRF analysis)**

150 The geochemical data were obtained by measuring the elemental composition of 566 samples,
151 using a NITON XL3t 900Analyzer with GOLDD Technology, placed in a Thermo Scientific portable
152 test stand. The samples were measured in Cu/Zn Mining Mode (Filters: Main 30, Low 30, High 30
153 and Light 60 seconds), with 2 control samples (NIST2780 and NIST2709a) measured every 9
154 samples. The elements measured with these settings are Zr, Sr, Fe, Al, Ca, Ti, Ba, Si, Mg, K, Nb,
155 Rb, Zn, Mn, V, Cl and S. A helium purge was used to obtain more accurate measurements for the
156 lighter elements (Mg, Al, Si, S). Homogeneous control samples were included in the measurements
157 to detect possible internal fluctuations related to the measuring equipment.

158 Analysis was done on a flat surface to prevent that unevenness of the sample disturbs the
159 measurements, thereby reducing their accuracy. All measurements were repeated three times at
160 different spot positions to correct for sample inhomogeneity; these measurements were averaged

161 to increase precision. Measurements were rejected and, if necessary, repeated, if the standard
162 deviation was too high compared to the measured value (>1.5 times 2σ).

163 The CaCO_3 content is calculated by multiplying the measured Ca concentration with a factor
164 2.496, assuming that all Ca present is bound by carbonate. The CaCO_3 content is presented in
165 ppm, where 1 billion ppm represents 100% CaCO_3 . Elemental proxy records were obtained by
166 normalizing the measured element with Al to correct for the detrital fraction (in case of redox-
167 sensitive and chalcophilic elements, such as V and Mo, and carbonate) and to reveal subtle
168 differences in concentrations that are not related to variation in clay content (in case of terrestrial
169 elements such as Fe, Ti and Zr) (e.g., Schenau et al. 1999). An exception is the calculated Rb/Sr
170 ratio.

171 **3.5. Statistical analysis (Student t Test)**

172 An Independent Student t Test was applied to selected planktonic foraminifer taxa and
173 geochemical elements in order to test if their variability is related to changes in sediment color.
174 This analysis is based on the comparison between mean values of the faunal and geochemical
175 proxies in two different main sediment colors (greenish gray and olive gray).

176 **3.6. Time series analysis**

177 Wavelet analysis was applied using the Torrence and Compo (1998) guide to detect changes in
178 the frequency-time domain that result from changes in sedimentation rate. The Blackman-Tukey
179 method in Analyseries (Paillard et al. 1996) was used for spectral analysis in combination with
180 bandpass filtering of the main frequency components.

181

182 **4. Results**

183 **4.1. Lithology**

184 The new composite section of the Lower La Vedova Beach section is about 63 m thick and
185 starts with Megabed II (Figs. 2 and 3), as Megabed I was not sampled because of poor outcrop
186 conditions. The lower 38 m of the section are characterized by Megabeds II to VII, which are
187 separated by less indurated, marl intervals. This large scale alternation of indurated limestone
188 intervals and marls continues well above Megabed VII despite the more marly character of the
189 succession; from 38 m up to the top of the section 6 additional indurated intervals (megabed VIII
190 to XIII) can be observed. The marl intervals between megabeds are characterized by intercalations
191 of brownish or greenish gray marls and limestone layers (less prominent and thick than in the
192 megabed intervals) and correspond mostly to the clustering of the greenish gray layers based on

193 the description of the fresh core color. These marl intervals are generally distinct, except for the
194 intervals between megabed II and III, VI and VII and X and XI which are only weakly expressed
195 (Figs. 2 and 3).

196 **4.2. Planktonic foraminifer proxies**

197 The distribution pattern of *Globigerinoides trilobus* gr. and *Globigerinoides*
198 *sicanus/Praeorbulina* gr. shows a rather consistent relationship with lithology (Fig. 3). These taxa
199 show abundance fluctuations, which follow the megabed/marl interval alternation rather well. In
200 particular, *G. trilobus* gr. is more abundant in the marl intervals between the megabeds (more
201 evident in the lower part of the section) than in the megabeds. Superimposed on this large scale
202 pattern, *G. trilobus* gr. often reveals abundance peaks in (or very close to) the greenish gray
203 layers, which occur in clusters mainly in the marl intervals, whereas it is less abundant in the olive
204 gray intervals. This relationship with sediment color is confirmed by the results of the Student t-
205 Test analysis, which show higher abundances of *G. trilobus* gr. and *G. sicanus/Praeorbulina* gr. in
206 the greenish gray layers (Tab. 2).

207 **4.3. Geophysical proxies (MS)**

208 Magnetic susceptibility (MS) is a sensitive indicator of changes in the marine sedimentary iron
209 concentrations (e.g., Hay 1996, 1998, Ellwood et al. 2000) and hence of variability in terrigenous
210 content, since iron is mainly supplied from land (Poulton and Raiswell 2002). MS record is shown in
211 Figure 4, together with its 3 and 5 point moving average (pma) to reduce the effect of high-
212 frequency variations and enhance regularities in the signal. MS record tracks the megabed/marl
213 interval alternation throughout the section, showing higher values in the marl intervals and lower
214 values in the megabeds (Fig. 4). This pattern is more evident in the lower 40 m of the section,
215 where the amplitude variation of the MS values between megabeds and marl intervals is more
216 pronounced.

217 **4.4. Geochemical proxies (XRF elemental record)**

218 Here we only present those elements or elemental ratios that are important for the tuning of
219 the Lower La Vedova Beach section and the understanding of the cycles: Al, CaCO₃, Ca/Al, Si/Al,
220 Rb/Sr, Rb/Al and Ti/Al. These records are shown in Figure 4, together with their 3 and 5 pma, and
221 the results of the Independent Student t Test are shown in Table 2.

222 Al is considered as an useful indicator of the terrestrial fraction since it mainly resides in clays
223 (e.g., Nijenhuis et al. 1996, Schenau et al. 1999). Al reveals distinct variations at the scale of
224 megabed/marl interval alternation with higher values in the marl intervals; these are more evident

225 in the true megabed interval in the lower part of the section. The amplitude variation of Al content
226 between megabeds and marl intervals shows an upward decreasing trend similarly to MS. In
227 addition, more prominent smaller-scale variations are observed in the upper half of the section.

228 The CaCO₃ record shows less distinct variations associated with the megabeds, but the marl
229 intervals in between the megabeds are often marked by regular high-amplitude variations on a
230 smaller-scale. Ca/Al reflects the relative carbonate content with respect to the input of clay
231 assuming that most of Ca is derived from calcium carbonate (e.g., Mourik et al. 2010). Ca/Al
232 record shows large-scale variations with maxima associated with the megabeds in the lower 20
233 meters of the section. Upwards, the record continues to show variations linked with the thinner
234 megabeds, but becomes dominated by more regular smaller-scale variations. Small scale maxima
235 of Ca/Al are statistically related to greenish gray layers (often limestones), as it is shown by
236 Student t Test analysis (Tab. 2).

237 The Si/Al record shows strong variations related to the true megabeds in the lower 40 m of the
238 section with distinct maxima associated with the megabeds. Similar variations, but with a much
239 smaller amplitude, can be recognized up to megabed XI above which the signal diminishes.
240 Superimposed on this large scale variability the record shows small scale variations, which are
241 related to sediment color, having lower values in the greenish gray layers and higher values in the
242 olive gray layers (Tab. 2).

243 Rb/Sr is considered as an indicator of chemical weathering intensity because Rb mainly occurs
244 in K-bearing minerals which are relatively resistant to weathering, and Sr remains in Ca-bearing
245 minerals which are sensitive to weathering (e.g., Chen et al 1999). Rb/Sr shows clear variations
246 related to the megabeds throughout the entire section with maxima in marl intervals. Regular
247 variations on a smaller-scale are evident in the 5-pma in middle part of the section (i.e., from 30 to
248 45m) and in the 3-pma in the upper 15 meters of the section.

249 The Rb/Al and Ti/Al records, the latter considered as an indicator of the aeolian terrestrial
250 fraction and then the wind-borne terrestrial input (e.g., Nijenhuis et al. 1996), do not clearly track
251 the megabed/marl interval alternations. On the contrary, they show regular small-scale variations
252 that are thicker in the lower 20 m and become thinner in the upper part of the section. Small scale
253 variations seem to be related to sediment color, showing lower values in the greenish gray layers
254 (Tab. 2).

255 **4.5. Time series analysis**

256 MS, Al, Ca/Al and Rb/Sr proved to be the most suitable records for time series analysis. All
257 wavelet spectra reveal the signature of a prominent ~ 7 m cycle in the lower 40 m of the section,
258 which corresponds to megabeds II-VII (Fig. 5). Upwards, a much less distinct 3-3.5 m cycle can be
259 recognized in the Al and Ca/Al wavelet spectra (Fig. 5), which may reflect the thinner megabeds
260 described from this part of the section. In addition, enhanced power maxima associated with a 0.5-
261 1.0 m cyclicity are recurrently observed between 40 and 63 m (Fig. 5).

262 The results of the wavelet analysis are confirmed by the outcome of the Blackman-Tukey
263 spectral analysis; the latter was run separately for the 0-40 and 40-63 m intervals to avoid
264 distortion caused by inferred changes in sedimentation rate suggested by the upward decrease in
265 the thickness of the megabeds, as confirmed by the outcome of the wavelet analysis. The spectra
266 of the two intervals reveal dominant peaks of ~ 7 and 3-3.5 m, respectively (Figs. 6 and 7). These
267 cycles correspond to the alternation of megabeds and marl intervals identified in the section and
268 show a similar decrease in thickness. The bandpass filtered ~ 7 m cycle in the lower part of the
269 section agrees well with the megabeds. The same holds for the filtered 3-3.5 m cycles in Rb/Sr in
270 the upper part of the section. However, in this part, the filtered MS, Al, and Ca/Al components
271 suggest that one or two extra cycles are present in the interval between 40 and 50 m. Spectra in
272 addition reveal peaks at higher frequencies that correspond to cycles with a thickness of ~ 1.5 and
273 ~ 0.7 m in the lower and upper part of the section, respectively (Figs. 6 and 7). Bandpass filtering
274 of these cycles, applied to Ca/Al, CaCO₃ and Rb/Al records, reveals amplitude variations often with
275 higher amplitudes in the marl intervals in between the megabeds (Fig. 8).

276

277 **5. Tuning and astronomical time scale**

278 **5.1. Tuning to eccentricity**

279 The calibration of the magnetostratigraphy to the polarity time scale of the ATNTS2012 (Hilgen
280 et al. 2012) (Fig. 3) suggests that the megabed scale alternations are related to the ~ 100 -kyr
281 eccentricity cycle with 10.5 alternations in 1.1 myr, between 16.268 (C5Cn.1n(o) at -2.90 m, Turco
282 et al. 2011a) and 15.160 Ma (C5Bn.2n(o) at 56.385 m, this paper). The same holds for the
283 associated 7 and 3-3.5 m cycles detected by time series analysis of the proxy records (Figs. 6 and
284 7). However, in order to establish a tuning, also the phase relation between the megabed/marl
285 interval alternations and eccentricity has to be known. In the Lower La Vedova Beach section the
286 records which better show a megabed scale variability throughout all the succession are those of

287 the *G. trilobus* gr., MS and Rb/Sr (Fig. 9). Following previously established phase relation between
288 these proxies and precession/eccentricity cycles (e.g., Zinsheng et al. 2001, Sprovieri et al. 2002)
289 maxima in the *G. trilobus* gr. (albeit less clear in the upper part of the section) MS, and Rb/Sr
290 suggest that the marl intervals in between the megabeds correspond to eccentricity maxima.
291 Consequently, megabeds correspond to eccentricity minima. A similar phase relation is also
292 suggested by the clusters of greenish gray layers and the preferentially higher amplitudes of the
293 filtered higher frequency proxy cycles occurring in the marl intervals (Fig. 8). In view of the ratio
294 thickness of the cyclicity, these high frequency cycles should correspond to precession and the
295 observed amplitude variations to the amplitude modulation of precession by eccentricity.

296 For the tuning to eccentricity, we preferred to start from the megabed/marl interval
297 alternations rather than to use the bandpass filtered components. The reason for this is that the
298 outcome of the bandpass filtering is complicated by the reduction in thickness of the megabed/marl
299 interval alternations in the section, supposedly reflecting a lowering of the sedimentation rate. This
300 reduction in thickness of the megabed scale cycles does not occur abruptly, but rather gradually
301 between 40 and 50 m, and may explain the one or two extra cycles that are observed in the
302 bandpass filtered components in MS, Al and Ca/Al in this interval.

303 The tuning can proceed from the top of the section downward, following the previously
304 established tuning of the younger Upper La Vedova Beach section (Hüsing et al. 2010) to which it
305 is stratigraphically connected. The top of the Lower La Vedova Beach section thus coincides with
306 the base of the distinctive interval with thinly bedded limestones that marks the 405-kyr
307 eccentricity minimum around 15.0 Ma (Hüsing et al. 2010). The megabeds XIII to II in our section
308 are tuned to successively older ~100-kyr eccentricity minima, following this 405-kyr minimum (Fig.
309 9). The resulting tuning is consistent with the weakly developed marl intervals between megabeds
310 X and XI, VI and VII, II and III, which mark the low amplitude ~100-kyr maxima in the 405-kyr
311 minima at 15.4 Ma, 15.8 and 16.2 Ma, respectively. The 3 distinct marl intervals between
312 megabeds XI and XIII, VII and IX, III and VI correspond to the three prominent ~100-kyr maxima
313 which denote the 405-kyr maximum around 15.2 Ma, 15.6 Ma and 16.00 Ma, respectively.
314 According to this tuning, the thick megabeds III and VII coincide with marked ~100-kyr minima at
315 16.13 and 15.75 Ma, while the thinner megabeds II and IV correspond to weak ~100-kyr minima.
316 Further constraints come from the tuning of the downward extension of our section near Ancona.
317 The elemental proxy records in this section reveal a marked increase in amplitude of the signal
318 associated with the precession related cyclicity. This increase logically reflects the 405-kyr

319 eccentricity maximum around 16.4 Ma marked by two distinct \sim 100-kyr maxima (unpublished
320 data). However, *G. trilobus* gr. MS and Rb/Sr maxima do not perfectly fit with the pattern of
321 eccentricity maxima (e.g., *G. trilobus* gr. pronounced maximum in the marl interval between
322 megabeds VI and VII which corresponds to a weak 100 kyr eccentricity maximum) (Fig. 9).

323 The tuning to eccentricity was used to establish a first order astronomical age model with two
324 tie-points per 100-kyr cycle. These tie-points were visually selected as the midpoints of the
325 calcareous and marl intervals of the cycles and tuned to the correlative minimum and maximum
326 eccentricity, respectively. This age model was used to establish eccentricity tuned time series for
327 the proxy records. Not surprisingly, spectral analyses of these time series revealed the presence of
328 a \sim 100-kyr eccentricity-related cycle as the proxy records have been tuned to eccentricity (Fig. 9).
329 This eccentricity related signal was extracted by means of bandpass filtering and is compared with
330 eccentricity in Figure 10. However, spectral analysis also detected precession-related variability
331 (Fig. 11). Bandpass filtering was applied to extract this signal from the Rb/Sr and Rb/Al time
332 series, which show this scale of cyclicity most clearly (Figure 11). All filtered components are
333 shown as overlay on the proxy records for direct comparison with the time series (Figs. 10 and 11).

334 **5.2. Tuning to precession and insolation**

335 The final age model is generated by the tuning of the high frequency cyclicity to precession and
336 65° Nlat summer insolation. The latter is widely used as target curve in the Mediterranean for
337 reasons outlined in Lourens et al. (1996) and provides a good fit with the cycle patterns. However,
338 a recent modeling study (Bosmans et al. 2015) suggests that better alternative target curves can
339 be used, as the forcing of both the precession and obliquity signal likely comes from low-latitudes,
340 although the insolation patterns remain essentially the same. For that reason, we will stick here to
341 the classical 65° Nlat summer insolation curve. For the tuning at the precession scale, again the
342 phase relation with the target curve(s) has to be known. However, the issue of the phase relation
343 of the cycles with precession and insolation has proven to be particularly challenging because the
344 structure of the basic cycle in the section is not clearly developed and the phase relation between
345 proxies and astronomical cycle may have changed over time. Following the Mi3b shift to heavy
346 values in $\delta^{18}\text{O}$ at 13.8 -13.9 Ma, which marks the end of the Middle Miocene Climate Transition and
347 the occurrence of the first sapropelitic layers in basic precession-controlled cycles typical of the
348 Mediterranean late Neogene (Mourik et al. 2010), the phase relation with precession and insolation
349 is relatively straightforward. Sapropels, associated with maxima in redox-sensitive elements (such
350 as V) and productivity indicator Ba/Al and with minima in aeolian terrestrial fraction indicators such

351 as Ti/Al and Zr/Al and Rb/Al (e.g., Nijenhuis et al. 1996, Schenau et al. 1999, Calvert and
352 Fontugne 2001), correspond to precession minima and obliquity maxima, and hence to (boreal)
353 summer insolation maxima. This phase relation remains remarkable constant up to the most recent
354 sediments deposited in the Mediterranean, although the youngest sapropels may reveal a time lag
355 of up to ~3 kyr relative to the astronomical forcing due to the influence of the ice ages and cold
356 climate phases, such as the Younger Dryas, that occur superimposed on deglaciations (Ziegler et
357 al. 2010). Sapropels are further often associated with maxima in the planktonic foraminifer
358 *Globigerinoides* spp. (Sprovieri 1992, Nijenhuis et al. 1996, Schenau et al. 1999, Sprovieri et al.
359 2006) and minima in both oxygen and carbon planktonic and bulk isotope values. On the contrary,
360 the phase relation between limestone beds (associated with Ca-maxima) and precession/insolation
361 is not constant. In the Pliocene Trubi Formation limestone beds correspond to precession
362 maxima/insolation minima (Hilgen 1991), whereas in the middle Miocene Monte dei Corvi beach
363 section limestone beds, in which sapropels tend to develop, correspond to precession
364 minima/insolation maxima (Hilgen et al. 2003).

365 In the La Vedova High Cliff section between 14.2 and 13.5 Ma, Mourik et al. (2010) consistently
366 tuned minima in the second principal component of the chemical elements (PC-2) to summer
367 insolation maxima (hence, precession minima), as PC-2 groups Ti/Al and Zr/Al on the positive side
368 opposite to redox-sensitive and chalcophile elements, such as V/Al, on the negative side. PC-2
369 minima further correspond to $\delta^{18}\text{O}$ and $\delta^{13}\text{C}$ minima. These relations are consistent with the
370 relations observed in younger marine successions in the Mediterranean (De Visser et al. 1989, Van
371 Os et al. 1994, Nijenhuis et al. 1996, Schenau et al. 1999, Wehausen and Brumsack 2000) and
372 with the tuning of sapropels (marked by Ti/Al and Zr/Al minima and V/Al maxima and occurring in
373 the upper part of the section above the Mi3b isotope shift) to summer insolation maxima. However,
374 close inspection of the data (Fig. 5 in Mourik et al. 2010) reveals that PC-2 minima (and hence
375 Ti/Al minima) in the interval older than 13.8 Ma mostly correspond to V/Al minima and Ca/Al
376 maxima, and to $\delta^{13}\text{C}$ and to a lesser extent $\delta^{18}\text{O}$ maxima.

377 This suggests that the relation between the proxies changes across the Mi3b $\delta^{18}\text{O}$ isotope shift,
378 although it is not abrupt. The relation observed below the Mi3b in the La Vedova High Cliff section
379 seems to be similar to that observed in the older Upper La Vedova Beach section (Hüsing et al.
380 2010) and in its downward extension (this paper). The question that remains is which phase
381 relations with precession and insolation remain constant and which phase relations become
382 opposite.

383 In the upper La Vedova Beach section between 15.29 and 14.17 Ma, Ca-maxima are often
384 associated with minima in MS and maxima in Ba/Al and V/Al, whereas their relationship with Ti/Al
385 and Zr/Al is not consistent throughout the entire section (Hüsing 2008, Hüsing et al. 2010). In her
386 PhD-thesis, Hüsing (2008) tuned limestone beds in the upper La Vedova Beach section to
387 precession minima/summer insolation maxima, as these beds are usually associated with V/Al and
388 Ba/Al maxima; this phase relation was based on the assumption that the expression of sapropels is
389 lacking, but that associated reducing conditions are still expressed as V/Al maxima. In the lower
390 part of the section, maxima of these proxies occur often just below the limestone beds, but this
391 was explained by assuming that only the upper limestone bed of the quadruplet structure of the
392 precession-related cycles, as observed in the younger La Vedova High Cliff and Monte dei Corvi
393 section, is developed (see Fig. 2 in Hilgen et al. 2003). However, in the paper that was
394 subsequently published (Hüsing et al. 2010), the phase relation with precession and insolation
395 became opposite following suggestions by the referees as to conform shifts to heavier values of
396 bulk $\delta^{18}\text{O}$ and $\delta^{13}\text{C}$ isotopes observed in limestone beds (Mader et al. 2004). These limestone beds
397 were thus tuned to precession maxima/summer insolation minima.

398 In the lower La Vedova Beach section (this paper), the build-up of the basic cycles is not clearly
399 expressed even in the marl intervals, between the megabeds, corresponding to 100 kyr eccentricity
400 maxima. However, the core color record shows that the greenish gray layers are intercalated in the
401 predominant olive gray sediments; these layers are composed of marls or marls associated with a
402 limestone bed at the base or at the top. The clustering of these greenish gray layers in the marl
403 intervals corresponding to 100 kyr eccentricity maxima, suggests that they can be the expression
404 of the precession scale cyclicity. This high frequency cyclicity is also portrayed by the proxy records
405 as MS, Rb/Sr, Ti/Al, Rb/Al and Ca/Al (Fig. 12). In particular, minima in Ti/Al, Rb/Al, Rb/Sr and MS,
406 and maxima in Ca/Al are generally found in the greenish gray layers. These layers are also
407 associated with maxima in the *G. trilobus* gr. (Tab. 2). Assuming that the phase relation of the
408 terrestrial fraction indicators and *Globigerinoides* with precession/insolation cycles remains
409 constant, then minima in Ti/Al, Rb/Al, Rb/Sr and MS and associated maxima in Ca/Al correspond to
410 precession minima/insolation maxima, of which the greenish gray layers are the lithological
411 expression. Assuming this phase relation we tuned the section to the Laskar2004_(1,1) insolation
412 target curve (Fig. 12). The starting point was the tuning of the megabed/marl interval alternations
413 to eccentricity with the marl intervals corresponding to 100 kyr maxima and the megabeds to the
414 100 kyr minima (Fig. 9). First we tuned the precession scale cycles in marly intervals to high

415 amplitude insolation cycles in the correlative 100-kyr eccentricity maximum. The tuning was then
416 expanded by correlating precession scale cycles in the megabeds to low amplitude insolation cycles
417 in the correlative 100 kyr eccentricity minimum (Fig. 12). The tie points used for the tuning to
418 insolation curve are indicated by crosses and were selected considering the high frequency
419 variability of all the proxies (Fig. 12).

420 However, in view of the uncertainties of the phase relation between Ca-maxima and
421 precession/insolation cycles (e.g., Mader et al. 2004, Husing et al. 2010) we also prepared a tuning
422 based on the opposite phase relation (Supplementary material B, Fig. B1).

423

424 **6. DISCUSSION**

425 **6.1. Magnetobiostratigraphy and astronomical calibration**

426 The tuning results in astronomical ages for magnetic reversal boundaries and calcareous
427 plankton events recorded in the Lower La Vedova section. These events were calibrated starting
428 from both the tuning to eccentricity and to insolation (Tab. 3). The ages for the C5Cn.1n/C5Br and
429 C5Br/C5Bn.2n boundaries are older than the ages for the same boundaries in the most recent
430 standard Geological Time Scale (ATNTS2012 of Hilgen et al. 2012), where they were calibrated by
431 means of interpolation of seafloor spreading rates using anomaly profiles from the Pacific. In the
432 Lower La Vedova Beach section the C5Cn.1n/C5Br boundary is dated 43/56 kyrs older than in
433 ATNTS2012 at 16.017/16.030 Ma; the age difference between our calibration and ATNTS2012 is
434 greater (104/91 kyrs) for the C5Br/C5Bn.2n boundary dated at 15.264/15.251 Ma (Tab.3). This
435 age discrepancy does not seem to be due to tuning problems, since the tuning of the Lower La
436 Vedova Beach section is consistent with the tuning of the younger Upper La Vedova Beach section
437 of Husing et al. (2010) and the succession below the megabed interval as exposed in sections near
438 Ancona (unpublished data).

439 The astronomical ages for the calcareous plankton events (based on the tuning to eccentricity
440 and to insolation) are presented in Table 3 and compared with the magnetostratigraphic ages
441 according to the revised age model of Turco et al. (2011a) in this study. The astronomical ages are
442 different with age discrepancies up to ~50 kyr for the bioevents recorded in the short normal
443 polarity intervals (C5Cn.1n and C5Bn.2n) and up to 200 kyr for the bioevents associated with the
444 long reversed interval (C5Br). The astronomical ages should be considered more reliable than the
445 magnetostratigraphic ages for several reasons. In the first place, the tuning is likely correct on the
446 eccentricity scale, based on the agreement between the cycle pattern and the eccentricity target

447 curve. Secondly, the number of tie-points in the magnetostratigraphic age model is limited so that
448 constant sedimentation rates had to be inferred over prolonged stratigraphic intervals, while the
449 thinning of the megabeds suggests a reduction in sedimentation rate in the middle reversed part of
450 the section.

451 The integrated magnetobiostratigraphy and tuning of the La Vedova section can be best
452 compared with that of the Moria section. The latter section has not been tuned, but a
453 magnetobiostratigraphy and single crystal $^{39}\text{Ar}/^{40}\text{Ar}$ dates for several ash-beds are available (Deino
454 et al. 1997, Di Stefano et al. 2008). The $^{39}\text{Ar}/^{40}\text{Ar}$ ages were calculated, using an age of 27.84 Ma
455 for the Fish Canyon sanidine (FCs) dating standard, but have been recalculated relative to the
456 astronomically calibrated FCs age of 28.201 Ma (Kuiper et al. 2008) for direct comparison with our
457 astronomical tuning of La Vedova. The two youngest of the three ash-beds dated in the Moria
458 section by Deino et al. (1997) are relevant for our study. They are intercalated in the Siliceous-
459 Calcareous Member of the Schlier Formation, which corresponds to the interval of the Massive
460 Member marked by the seven Megabeds at La Vedova. The base of the *Sphenolithus*
461 *heteromorphus* Paracme and the second influx of *Globoturbotalita woodi* are respectively found
462 directly below or nearly coincident with the top of these stratigraphic intervals, indicating that this
463 level is synchronous between the sections (Deino et al. 1997, Di Stefano et al. 2008, Turco et al.
464 2011a). However, it is not clear whether the base of these members is also synchronous in the two
465 sections, due to lack of high-resolution biostratigraphic control in this interval.

466 The stratigraphic position of the youngest dated Moria ash-bed (76.8 m in the section of Deino
467 et al. 1997 corresponding to the level of 28 m in the section of Di Stefano et al. 2008) is close to
468 the top of the Siliceous-Calcareous member, just below the base of the *S. heteromorphus* Paracme
469 and the second influx of *G. woodi* (Deino et al. 1997, Di Stefano et al. 2008, Turco et al. 2011a).
470 This suggests that this ash-bed corresponds with the younger of the two newly detected ash-beds
471 at La Vedova (Fig. 3). Unfortunately, the age of the Moria ash-bed is complicated by a bimodal age
472 distribution, but its recalculated age of 15.70 ± 0.16 Ma is nevertheless within error consistent with
473 the estimated astronomical age of ~ 15.75 Ma at La Vedova (Fig. 9). The other dated Moria ash-bed
474 of interest is located at 58.4 m in the section of Deino et al. (1997). In view of the stratigraphic
475 thickness, it is likely that this Moria ash-bed corresponds to one out of two ash-beds found at ~ 13
476 and 11 m in the Moria section of Di Stefano et al. (2008). Both ash-beds are intercalated well
477 below the *Helicosphaera ampliapertura* LCO (Di Stefano et al. 2008). Downward extrapolation of the
478 sedimentation rate, using the astronomical ages of the first influx base of *G. woodi* gr. (16.014 Ma)

479 and the *H. ampliaperta* LCO (16.094 Ma), results in an age of ~16.25 Ma and 16.33 Ma,
480 respectively, for these ash layers. These ages are within error consistent with the recalculated
481 single crystal $^{40}\text{Ar}/^{39}\text{Ar}$ sanidine age of 16.39 ± 0.16 Ma, and again in agreement with our tuning.
482 The detailed comparison further reveals that the magnetostratigraphy of the La Moria section and
483 its calibration to the polarity time scale is likely flawed.

484 Alternatively, our tuning may be put to the test through radio-isotopic dating of the Columbia
485 River Basalt Group (CRBG), including Steens Mountain, in North America. This basalt succession
486 covers the critical interval of the Middle Miocene and has a clear magnetostratigraphy in terms of
487 N0 through R2 polarity intervals. Initial $^{40}\text{Ar}/^{39}\text{Ar}$ ages (Baksi and Farrer 1990) are inconsistent
488 with the astronomical ages for the chron boundaries unless the chron assignment of the CRBG
489 magnetostratigraphy is wrong. However, these ages are based on bulk samples and considered
490 less reliable for several reasons (Jarboe et al. 2008, 2010). Ages in the latter study are consistent
491 with the ATNTS2004/2012, but the ages in this interval of the ATNTS are still determined with the -
492 additional - help of seafloor anomaly profiles. On the contrary, the ages of Barry et al. (2010) are
493 once more inconsistent with our ages, but errors are large and again the reliability of the data has
494 been debated (Baksi 2012, Barry et al. 2012, 2013). For the moment, $^{40}\text{Ar}/^{39}\text{Ar}$ ages of the CRBG
495 cannot be used with confidence to test our tuning, as the reliability of these ages is not clear at
496 present.

497 **6.2. Phase relations**

498 The problem of the phase relation with precession and insolation is fundamental but complex.
499 Evidently, the relation between the proxies changes across the Mi3b event and, thus, the
500 associated glacio-eustatic sea-level lowering and/or climate changes were likely responsible for this
501 change. If we assume that prior of Mi3b event the phase relation between Ca/Al, V/Al, Ti/Al and
502 Zr/Al with precession remained constant then the phase relation with the oxygen and carbon bulk
503 isotopes will become opposite. In that case, Ca/Al and V/Al maxima, and Ti/Al and Zr/Al minima
504 correspond to precession minima and summer insolation maxima, just as is the case for the
505 interval younger than the Mi3b. The V/Al maxima may point to reducing conditions, but sapropels
506 were not developed. Note, however, that the distinct quadripartite structure of the precession
507 related cycles above the Mi3b event with the development of sapropels in the limestone beds
508 complicates the relation between Ca/Al maxima and precession minima. In the presently studied
509 section, the greenish gray marl/limestones show the same phase relation, being characterized by
510 Ca/Al maxima and Ti/Al and Zr/Al minima, although V/Al does not show an univocal relationship

511 with these layers (Tab. 2). The Ti/Al and Zr/Al minima can be explained by an enhanced fluvial
512 signal, while the maxima in the opposite phase of the cycle point to a relatively larger input of
513 eolian material. Sapropels only develop after the Mi3b, suggesting an intensification of the African
514 monsoon or, alternatively, that this part of the Mediterranean became more enclosed, possibly as a
515 consequence of the sea-level lowering associated with the Mi3b, and, therefore, more sensitive to
516 monsoonal induced climate variability. This may also explain why the isotope shifts to lighter
517 values associated with the sapropels only started to be recorded above the Mi3b. Before the Mi3b
518 the $\delta^{18}\text{O}$ shifts to heavier values in the limestone beds may be explained by the fact that they do
519 not record the summer signal with the stronger heating and enhanced outflow of fluvial run-off, but
520 instead the colder winters which are also associated with precession minima.

521 According to this scenario, the limestone, or Ca/Al maxima, correspond to the basic
522 couplet/doublet limestone-marl cycle as depicted in Hilgen et al. (2003, their Fig. 2) with sapropels
523 starting to be intercalated in the limestone beds above the Mi3b during eccentricity maxima when
524 precession amplitudes are enlarged, resulting in the characteristic quadruplet structure of the
525 cycles in the upper part of the La Vedova High Cliff and lower part of the Monte dei Corvi sections.
526 According to the alternative scenario, the phase relation between limestone beds, or Ca/Al
527 maxima, would become opposite across the Mi3b. The limestone beds and intercalated sapropels
528 correspond to precession minima from ~ 13.8 Ma onwards, while they correspond to precession
529 maxima in older intervals. For the moment we consider the first option with the limestones beds
530 and associated maxima in Ca/Al and *G. trilobus* gr. and minima in Ti/Al and Zr/Al corresponding to
531 precession minima more likely as that implies less drastic changes in the underlying climate
532 changes.

533 The discussion about the precession (and obliquity) phase relation has major consequences for
534 attempts to reconstruct the tidal dissipation (TD) and dynamical ellipticity (DE) values in the
535 astronomical solution through detailed comparison with the cyclostratigraphic record (see Zeeden
536 et al. 2014). In particular, the (Upper) La Vedova Beach section of Hüsing et al. (2010) reveals
537 intricate precession-obliquity interference patterns that are suitable for the purpose. In that paper,
538 a TD value of 0.9 results in a good visual fit with the intricate cycle patterns, while in Hüsing
539 (2008) a value of ~ 1.2 is favored as a consequence of the preferred opposite phase relations (the
540 patterns in the insolation target curve essentially becomes mirrored) around 14.4 Ma. This value is
541 similar to the one that has been inferred for the lower part of the Monte dei Corvi section (Hilgen et
542 al. 2003, Hüsing et al. 2007). Thus the problem of the phase relation has to be solved before TD-

543 DE values can be reliably established. This is critical for comparison with studies that use models of
544 ice volume and mantle convection for reconstructing the TD – DE (Morrow et al. 2012). In view of
545 these uncertainties, we preferred to use the Laskar2004 astronomical solution with present day
546 values of TD and DE (Laskar 2004_(1,1)) in the present study.

547 **6.3. Origin of megabeds**

548 **6.3.1. Very long period astronomical cycles and the MMCO**

549 The magnetobiostratigraphic age constraints indicate that the megabeds are related to the
550 ~100-kyr eccentricity cycle and that the megabed interval (I-VII) corresponds to two successive
551 405-kyr eccentricity minima and the maximum in between. The limestone part of a cycle
552 (megabed) corresponds to ~100-kyr minimum and the marly interval to ~100-kyr maximum. The
553 expression of megabeds continues up to the top of the section, although these younger cycles are
554 much less indurated and have a more marly appearance. Nevertheless, the true megabeds I-VII
555 are not well expressed in the CaCO₃ content, but in Si/Al (Fig. 4). The indurated character of these
556 beds may thus be explained by an increase in Si rather than in CaCO₃ content. Remarkably, the
557 sedimentation rate is significantly reduced in the upper part of the section which on average has a
558 lower carbonate content. The higher sedimentation rate in the lower part may be related to the
559 increase in Si content observed in the true megabeds (Fig. 4). This Si is likely of biogenic origin
560 and may represent an intermittent decrease in Si content compared to the older Bisciario Formation
561 that is found stratigraphically ~65 m below the megabeds in coastal cliff sections near Ancona. This
562 unit is composed of marls and limestones with a high volcanoclastic component. Nevertheless, the
563 Si in the Bisciario Fm is mainly of biogenic origin, although diagenesis has altered the original opal-
564 CT into microcrystalline quartz (Morandi and Tateo 1992). In the world oceans, a positive
565 correlation is often found between sediment accumulation rate and biogenic silica preservation
566 (e.g., De Master et al. 1996, Ragueneau et al. 2000). In these cases, it is inferred that the higher
567 accumulation rate has contributed to enhanced biogenic silica preservation efficiency, but the
568 additional preservation of biogenic silica will also result in higher sedimentation rates.

569 The expression and amplitude of the small-scale precession related cycles is reduced in the
570 megabed interval. This suggests that this interval may correspond to a minimum in the 2.4 myr
571 eccentricity cycle, when precession amplitude is reduced as a consequence of minimum eccentricity
572 over a prolonged interval of time. However, these minima are reached at 14.2 and 16.6 Ma, thus
573 excluding a link to this very long period eccentricity cycle. Also a relation with the shorter 1.0 myr
574 eccentricity cycle is not evident.

575 The megabed interval between 16.3 to 15.7 Ma encompasses a minimum (node) in the 1.2 myr
576 obliquity cycle, in which the Mi2 glacial is placed at around 16 Ma (Fig. 5 in Boulila et al. 2011).
577 However, it is not clear how such an obliquity node and associated, but much shorter, glacial
578 episode may have affected the Mediterranean, as cycle patterns are dominated by the combination
579 of eccentricity and precession, and the top and bottom of the megabed interval are controlled by
580 successive minima of the 405-kyr eccentricity cycle. Also a relation with eustatic sea-level is not
581 clear, as the interval does not coincide with a marked sea-level high- (or low) stand (Haq et al.
582 1987, Miller et al. 2005).

583 Alternatively, one may argue that the megabed interval marks the acme of the MMCO. The
584 MMCO stretches from 17 to 15.0 Ma, just before the cooling trend towards the Mi3b isotope event
585 starts. High-resolution climate proxy records from the open ocean do not reveal that the interval
586 between 15.7 and 16.3 Ma is represented by a climax phase of the MMCO (Holbourn et al. 2007).

587 **6.3.2. Langhian transgression and tectonics**

588 Another option is that the megabed interval is related to the so-called Langhian transgression
589 that occurred widespread in the circum-Mediterranean region, including the Paratethys (base
590 Badenian) (e.g., Rögl 1998). This transgression, which is supposed to correspond to the
591 *Praeorbulina* event, may have led to a restoration of the connection with the Indian Ocean,
592 resulting in the migration of sub-tropical faunal elements into the Mediterranean-Paratethys area
593 (Rögl 1998).

594 But what is the age of the Langhian transgression? On Tremiti Islands (Adriatic Sea) this
595 transgression is documented by the sedimentation of shallow marine glauconitic sands which overly
596 Eocene limestones with an angular unconformity. The deep marine (hemi-)pelagic sedimentation
597 starts below the Acme_a of *Paragloborotalia siakensis* in the middle of the *S. heteromorphus*
598 Paracme (Di Stefano et al. 2008). The base of *P. siakensis* Acme_a and the *S. heteromorphus*
599 Paracme have estimated ages of 15.48 and 15.74 Ma respectively (Tab. 3). This suggests that the
600 local onset of marine sedimentation on Tremiti Islands may correspond to the top of the megabed
601 interval at La Vedova. The Langhian transgression supposedly has a tectonic origin (Rögl 1998)
602 and, in case of Tremiti Islands, may reflect deepening of the foreland basin, as a consequence of
603 thrust loading, due to the rapidly advancing orogenic front. In that case, the megabeds at La
604 Vedova may be associated with a phase of tectonic quiescence in the evolving orogen.

605 During the Neogene, the Apennine system migrated northeastwards with the marly Schlier
606 Formation and turbiditic Marnosa-Arenacea Fm becoming progressively younger towards the NE

607 (e.g., Boccaletti et al. 1990). Tectonic phases are supposed to be reflected in the internal
608 subdivision of the Schlier Formation (e.g., Guerrera et al. 2012). The Marnosa-Arenacea Fm is
609 characterized by the occurrence of marly members deposited on top of the turbidites of the
610 formation, reflecting the - local - end of turbidite deposition and, potentially, orogenic phases of
611 the Apenninic system (Ricci Lucchi and Ori 1985, Guerrera et al. 2012). However, the exact
612 relation of these members with the Schlier succession exposed in the La Vedova section is not
613 clear.

614 Interestingly, Böhme (2003), studying thermophilic ectothermic vertebrates from the Middle
615 Miocene of Central Europe, describes a first phase of enhanced seasonality especially in
616 precipitation between 16.3 and 15.7 Ma, i.e. almost exactly the interval of megabed formation. The
617 author relates this to a tectonic re-organization of the Central Paratethys realm, with subduction of
618 the North European platform and back-arc extension leading to extensive volcanism and the
619 formation of a volcanic belt, which may have affected regional atmospheric circulation. In this
620 particular case, the absence of a relation with long period eccentricity is remarkable as eccentricity
621 modulates the precession amplitude and, hence, has a strong effect on seasonality. The enhanced
622 volcanic activity may also have contributed to the deposition of sediments enriched in biogenic
623 silica in the megabed interval. Washed residues reveal a strong reduction in the amount of
624 foraminifera, suggesting that the biogenic silica producing system was unfavorable for the
625 foraminifera, and the presence of radiolarians within Megabed VII (33-35 m).

626 On the other hand, such a regional tectonic scenario in general would explain why this interval
627 is not related to any of the very long period eccentricity (or obliquity) cycles as discussed before,
628 although a strong control by the 405-kyr eccentricity cycle is evident.

629 **6.4. Langhian GSSP**

630 The Lower La Vedova Beach section is one of two candidate sections for defining the base of
631 the Langhian in the Mediterranean (Iaccarino et al. 2011). The magnetobiostratigraphy, previously
632 published (Turco et al. 2011a) and here revised (Fig. 3), shows that the succession is continuous
633 across the Burdigalian/Langhian boundary. Moreover, the recommended guiding criteria to identify
634 the base of the Langhian - the *Praeorbulina* datum (i.e., *P. glomerosa curva* FO following Turco et
635 al. 2011b) and the top of Chron C5Cn - are both recorded in the section (Iaccarino et al. 2011,
636 Turco et al. 2011a, Turco et al. 2011b, this paper).

637 Important extra criteria for defining GSSPs in the Neogene are that the section should be
638 astronomically tuned and contain the entire stage in a continuous marine section, representing a

639 unit stratotype for the stage in addition to the GSSP (Hilgen et al. 2006). The tuning of the Lower
640 La Vedova Beach section seems correct at the eccentricity scale, while is less straightforward on
641 the precession scale, as the expression of the basic precession related cycles is not always clear.
642 This is especially evident in the megabed interval that spans the boundary interval, if one prefers
643 to define the boundary close to or at the magnetic reversal associated with the younger end of
644 C5Cn. In addition, the cliffs of La Vedova contain the entire Langhian stage in an essentially
645 continuous and well-tuned succession, from its top as recorded in the La Vedova High Cliff section
646 (Mourik et al. 2010) to its base in the section presented in this paper (Hüsing et al. 2010, Turco et
647 al. 2011a, this paper); the entire La Vedova composite section can thus serve as a unit stratotype
648 for the Langhian. The Lower La Vedova Beach section is in principle suitable to define the GSSP, as
649 it meets the main selection criteria, although the magnetostratigraphy is of sufficient quality to
650 determine the position of the reversals and the biostratigraphy is affected by the moderate to poor
651 preservation of the calcareous plankton. This was the case for some other deep marine sections in
652 the Mediterranean that have been chosen to define GSSPs (Castradori et al. 1998, Van Couvering
653 et al. 2000, Hilgen et al. 2005). Also the other main candidate section for defining the Langhian
654 GSSP, St. Peter's Pool on Malta, is altogether not ideal as boundary stratotype (Iaccarino et al.
655 2011). Preservation of the calcareous plankton is much better resulting in an excellent calcareous
656 plankton biostratigraphy, but the magnetostratigraphy is poor.

657 An alternative option would be to define the GSSP in a deep-sea core. Several (I)ODP sites
658 might be suitable for this purpose: ODP Site 926 (Ceara Rise, Equatorial Atlantic), ODP Site 1264
659 (Walvis Ridge, South Atlantic), ODP Site 1237 (south eastern Pacific), ODP 1146 (South China Sea)
660 and IODP Site U1338 (eastern equatorial Pacific). These sites contain the entire Langhian and are
661 provided with well-preserved calcareous plankton assemblages, stable isotope records, and/or
662 good magnetostratigraphy and astronomical calibration. Moreover, at Site 1146 the stable isotope
663 records are of exceptional quality, portraying the paleoclimatic history in great detail, with nine
664 405-kyr $\delta^{13}\text{C}$ cycles of the Monterey event between 13.6 and 17 Ma, and the distinct increase in
665 $\delta^{18}\text{O}$ associated with the Mi3b event that reflects a marked increase in Antarctic ice volume
666 (Holbourn et al. 2007).

667 One can further discuss the desirability of defining a GSSP in a deep-sea core far outside the
668 historical stratotype area of a stage, but with the progress in astronomical tuning, one can equally
669 well argue that GSSPs should be defined in the best possible section or core, as they define global
670 and not regional stages.

671

672 **7. Conclusions**

673 The magnetobiostratigraphy of the Lower La Vedova Beach section has been improved
674 compared to an earlier publication (Turco et al. 2011a) by taking a previously unnoticed fault into
675 account as a result of the better exposure conditions of the succession.

676 The magnetic susceptibility and the elemental records of the section have been tuned to
677 eccentricity and precession/insolation, providing astronomical ages for reversal boundaries and
678 calcareous plankton events for the interval between 16.3 and ~15 Ma.

679 The tuning to eccentricity seems to be robust (with the individual megabeds corresponding to
680 100 kyr eccentricity minima), while that to insolation is not always straightforward. The megabed
681 interval (II-VII) shows a relation with the 405 kyr eccentricity cycles, covering two 405-kyr
682 eccentricity minima and the maximum in between, but not with the long period eccentricity cycles.

683 The megabed interval (II-VII), between 16.2 and 15.7 Ma, is probably linked to a regional
684 tectonic activity and to the circum-Mediterranean Langhian transgression and may represent the
685 last phase of biogenic silica enrichment following the older Bisciaro Formation.

686 The Lower La Vedova Beach section meets key requirements for defining the Langhian GSSP,
687 i.e. the presence of the guiding criteria for its recognition (Top of Chron C5Cn and *Praeorbulina*
688 datum), the astronomical tuning and, together with the Upper La Vedova Beach and the La Vedova
689 High Cliff sections, the presence of the entire Langhian stage in a continuous and tuned succession.
690 However, the magnetobiostratigraphy is not of exceptional quality, the tuning to precession is not
691 always straightforward and the construction of reliable planktonic and benthic isotope records is
692 not possible, due to the moderate to poor preservation of the foraminifera.

693

694 **8. Acknowledgements**

695

696

697

698

699 **9. References**

- 700 Abels, H.A., Hilgen, F.J., Krijgsman, W., Kruk, R.W., Raffi, I., Turco, E., Zachariasse, W.J., 2005.
701 Long-period orbital control on middle Miocene global cooling: integrated stratigraphy and
702 astronomical tuning of the Blue Clay Formation on Malta. *Paleoceanography* 20, doi:10.1029/
703 2004PA001129.
- 704 Baksi, A.K., Farrer, E., 1990. Evidence for errors in the geomagnetic polarity time-scale at 17–15
705 Ma: $^{40}\text{Ar}/^{39}\text{Ar}$ dating of basalt from the Pacific northwest, USA. *Geophysical Research Letters*
706 17, 1117–1120.
- 707 Baksi, A.K., 2012. "New $^{40}\text{Ar}/^{39}\text{Ar}$ dating of the Grande Ronde lavas, Columbia River Basalts, USA:
708 implications for duration of flood basalt eruption episodes" by Barry et al. (2010) - Discussion.
709 *Lithos* 146-147, 293–299.
- 710 Barry, T.L., Self, S., Kelley, S.P., Reidel, S., Hooper, P., Widdowson, M., 2010. New $^{40}\text{Ar}/^{39}\text{Ar}$
711 dating of the Grande Ronde lavas, Columbia River Basalts, USA: implications for duration of
712 flood basalt eruption episodes. *Lithos* 118, 213–222.
- 713 Barry, T.L., Self, S., Kelley, S.P., Reidel, S., Hooper, P., Widdowson, M., 2012. Response to Baksi,
714 A., 2012, 'New $^{40}\text{Ar}/^{39}\text{Ar}$ dating of the Grande Ronde lavas, Columbia river basalts, USA:
715 Implications for duration of flood basalt eruption episodes' by Barry et al., 2010 – discussion'.
716 *Lithos* 146-147, 300–303.
- 717 Barry, T.L., Kelley, S.P., Reidel, S.P., Camp, V.E., Self, S., Jarboe, N.A., Duncan, R.A., Renne, P.R.,
718 2013. Eruption Chronology of the Columbia River Basalt Group. Geological Society of America,
719 Special Paper 497, 45–66.
- 720 Boccaletti, M., Calamita, F., Deiana, G., Gelati, R., Massari, F., Moratti, G., Ricci Lucchi, F., 1990.
721 Migrating foredeep-thrust belt system in the Northern Apennines and Southern Alps.
722 *Palaeogeography Palaeoclimatology Palaeoecology* 77, 3–14.
- 723 Böhme, M., 2003. The Miocene climatic optimum: Evidence from ectothermic vertebrates of central
724 Europe. *Palaeogeography Palaeoclimatology Palaeoecology* 195, 389–401.
- 725 Bosmans, J.H.C., Hilgen, F.J., Tüenter, E., Lourens, L.J., 2015. Obliquity forcing of low-latitude
726 climate. *Climate of Past*, 11, 1335-1346.
- 727 Boulila, S., Galbrun, B., Miller, K.G., Pekar, S.F., Browning, J.V., Laskar, J., Wright, J.D., 2011. On
728 the origin of Cenozoic and Mesozoic "third-order" eustatic sequences. *Earth-Science Reviews*
729 109, 94–112.

730 Calvert, S.E., Fontugne, M.R., 2001. On the late Pleistocene-Holocene sapropel record of climatic
731 and oceanographic variability in the eastern Mediterranean. *Paleoceanography* 16, 78-94.

732 Castradori, D., Rio, D., Hilgen, F.J., Lourens, L.J., 1998. The Global Standard Stratotype-section
733 and Point (GSSP) of the Piacenzian Stage (Middle Pliocene). *Episodes* 21, 88-93.

734 Chen, J., Zhisheng, A., Head, J., 1999. Variation of Rb/Sr Ratios in the Loess-Paleosol Sequences
735 of Central China during the Last 130,000 Years and Their Implication for Monsoon
736 Paleoclimatology. *Quaternary Research*, 51, 215-219.

737 Deino, A., Channell, J., Coccioni, R., De Grandis, G., De Paolo, D. J., Fornaciari, E., Emmanuel, L.,
738 Laurenzi, M. A., Montanari, A., Rio, D., Renard, M., 1997. Integrated stratigraphy of the upper
739 Burdigalian-lower Langhian section at Moria (Marche Region, Italy). In: Montanari, A., Odin,
740 G.S., Coccioni, R. (Eds.), *Miocene stratigraphy: An integrated approach*. Developments in
741 *Palaeontology and Stratigraphy* 15, Elsevier, Amsterdam, p. 315-341.

742 De Master, D.J., Ragueneau, O., Nittrouer, C.A., 1996. Preservation efficiencies and accumulation
743 rates for biogenic silica and organic C, N, and P in high-latitude sediments: The Ross Sea.
744 *Journal Of Geophysical Research* 101, C8, 18.501-18.518.

745 De Visser, J.P., Ebbing, J.H.J., Gudjonsson, L., Hilgen, F.J., Jorissen, F.J., Verhallen, P.J.J.M.,
746 Zevenboom, D., 1989. The origin of rhythmic bedding in the Pliocene Trubi Formation of Sicily,
747 southern Italy. *Palaeogeography Palaeoclimatology Palaeoecology* 69, 45-66.

748 Di Stefano, A., Foresi, L.M., Lirer, F., Iaccarino, S.M., Turco, E., Amore, F.O., Mazzei, R., Morabito,
749 S., Salvatorini, G., Abdul Aziz, H.A., 2008. Calcareous plankton high resolution bio-
750 magnetostratigraphy for the Langhian of the Mediterranean area. *Rivista Italiana di*
751 *Paleontologia e Stratigrafia* 11, 51-76.

752 Ellwood, B.B., Crick, R.E., El Hassani, A., Benoist, S.L., Young, R.H., 2000. Magnetosusceptibility
753 event and cyclostratigraphy method applied to marine rocks; detrital input versus carbonate
754 productivity. *Geology*, 28, 1135-1138.

755 Foresi, L.M., Verducci, M., Baldassini, N., Lirer, F., Mazzei, R., Salvatorini, G., Ferraro, L., Da Prato,
756 S., 2011. Integrated stratigraphy of St. Peter's Pool section (Malta): new age for the Upper
757 Globigerina Limestone Member and progress towards the Langhian GSSP. *Stratigraphy* 8,
758 125-143.

759 Fornaciari, E., Di Stefano, A., Rio, D., Negri, A., 1996. Middle Miocene quantitative calcareous
760 nanofossil biostratigraphy in the Mediterranean region. *Micropaleontology* 42, 37-63.

761 Goddard, E.N, Trask, P.D., De Ford, R.K., Rowe, O.N., Singewald, J.T., Overbeck, R.M, 1963. Rock
762 Color Chart. Boulder: Geological Society of America.

763 Guerrera, F., Tramontana, M., Donatelli, U., Serrano, F., 2012. Space/time tectono-sedimentary
764 evolution of the Umbria-Romagna-Marche Miocene basin (northern Apennines, Italy): A
765 foredeep model. *Swiss Journal of Geosciences* 105, 325–341.

766 Haq, B.U., Hardenbol, J., Vail, P.R., 1987. Chronology of fluctuating sea levels since the Triassic.
767 *Science* 235, 1156–1167.

768 Hay, W.W., 1996. Tectonics and climate. *Geologische Rundschau* 85, 409–437.

769 Hay, W.W., 1998. Detrital sediment fluxes from continents to oceans. *Chemical Geology* 145, 287–
770 323.

771 Hilgen, F.J, 1991. Extension of the astronomically calibrated (polarity) time scale to the
772 Miocene/Pliocene boundary. *Earth and Planetary Science Letters* 107, 349–368.

773 Hilgen, F., Abdul Aziz, H., Bice, D., Iaccarino, S., Krijgsman, W., Kuiper, K., Montanari, A., Raffi, I.,
774 Turco, E., Zachariasse, W.-J., 2005. The global boundary stratotype section and point (GSSP)
775 of the Tortonian stage (upper Miocene) at Monte dei Corvi. *Episodes* 28, 6–17.

776 Hilgen, F.J., Abdul Aziz, H.A., Krijgsman, W., Raffi, I., Turco, E., 2003. Integrated stratigraphy and
777 astronomical tuning of the Serravallian and lower Tortonian at Monte dei Corvi (Middle–Upper
778 Miocene, northern Italy). *Palaeogeography Palaeoclimatology Palaeoecology* 199, 229–264.

779 Hilgen, F., Brinkhuis, H., Zachariasse, W.-J., 2006. Unit stratotypes for global stages: the Neogene
780 perspective. *Earth-Science Reviews* 74, 113–125.

781 Hilgen, F.J., Lourens, L.J., van Dam, J.A., 2012. The Neogene Period. In: Gradstein, F., Ogg, J.,
782 Schmitz, M., Ogg, G. (Eds.), *The Geological Time Scale 2012*. Elsevier, Amsterdam, p. 923–
783 978.

784 Holbourn, A., Kuhnt, W., Schulz, M., Erlenkeuser, H., 2005. Impacts of orbital forcing and
785 atmospheric carbon dioxide on Miocene ice-sheet expansion. *Nature* 438, 483–487.

786 Holbourn, A., Kuhnt, W., Schulz, M., Flores, J.-A., Andersen, N., 2007. Orbitally-paced climate
787 evolution during the middle Miocene "Monterey" carbon-isotope excursion. *Earth and Planetary
788 Science Letters* 261, 534–550.

789 Holbourn, A., Kuhnt, W., Clemens, S., Prell, W., Andersen, N., 2013. Middle to late Miocene
790 stepwise climate cooling: Evidence from a high-resolution deep water isotope curve spanning
791 8 million years. *Paleoceanography* 28, 688–699.

792 Holbourn, A, Kuhnt, W., Lyle, M., Schneider, L., Romero, O., Andersen, 2014. Middle Miocene
793 climate cooling linked to intensification of eastern equatorial Pacific upwelling. *Geology* 42, 19-
794 22.

795 Hüsing, S.K., 2008. Astrochronology of the Mediterranean Miocene: Linking palaeoenvironmental
796 changes to gateway dynamics. PhD thesis, *Geologica ultraiectina*, Utrecht University, 295 pp.

797 Hüsing, S.K., Hilgen, F.J., Abdul Aziz, H., Krijgsman, W., 2007. Completing the Neogene geological
798 time scale between 8.5 and 12.5 Ma. *Earth and Planetary Science Letters* 253, 340–358.

799 Hüsing, S.K., Hilgen, F.J., Kuiper, K.F., Krijgsman, W., Turco, E., Cascella, A., Wilson, D., 2010.
800 Astrochronology of the Mediterranean Langhian between 15.29 and 14.17 Ma. *Earth and*
801 *Planetary Science Letters* 290, 254–269.

802 Iaccarino, S., 1985. Mediterranean Miocene and Pliocene planktic foraminifera. In: Bolli, H.M.,
803 Saunders, J.B., Perch-Nielsen, K.(Eds.), *Plankton stratigraphy*, Cambridge University Press,
804 Cambridge, p. 283–314.

805 Iaccarino, S., Salvatorini, G., 1982. A framework of planktonic foraminifera biostratigraphy for
806 early Miocene to Late Pliocene Mediterranean area. *Paleontologia Stratigrafica ed Evoluzione* 2,
807 115–125.

808 Iaccarino, S., Di Stefano, A., Foresi, L.M., Turco, E., Baldassini, N., Cascella, A., Da Prato S.,
809 Ferraro, L., Gennari, R., Hilgen, F.J., Lirer, F., Maniscalco, R., Mazzei, R., Riforgiato, F., Russo,
810 B., Sagnotti, L., Salvatorini, G., Speranza, F., Verducci, M., 2011. High-resolution integrated
811 stratigraphy of the upper Burdigalian–lower Langhian in the Mediterranean: the Langhian
812 historical stratotype and new candidate sections for defining its GSSP. *Stratigraphy* 8, 199–
813 215.

814 Jarboe, N.A., Coe, R.S., Renne, P.R., Glen, J.M.G., Mankinen, E.A., 2008. Quickly erupted volcanic
815 sections of the Steens Basalt, Columbia River Basalt Group: Secular variation, tectonic
816 rotation, and the Steens Mountain reversal: *Geochemistry Geophysics. Geosystems* 9,
817 doi:10.1029/2008GC002067.

818 Jarboe, N.A., Coe, R.S, Renne, P.R., Glen, J.M.G., 2010. The age of the Steens reversal and the
819 Columbia River Basalt Group. *Chemical Geology* 274, 158–168.

820 Kuiper, K.F., Deino, A., Hilgen, F.J., Krijgsman, W., Renne, P.R., Wijbrans, J.R., 2008.
821 Synchronizing rock clocks of Earth history. *Science* 320, 500–504.

822 Laskar, J., Robutel, P., Joutel, F., Gastineau, M., Correia, A.C.M., Levrard, B., 2004. A long term
823 numerical solution for the insolation quantities of the Earth. *Astronomy and Astrophysics* 428,
824 261–285.

825 Lourens, L.J., Antonarakou, A., Hilgen, F.J., Van Hoof, A.A.M., Vergnaud-Grazzini, C., Zachariasse,
826 W.J., 1996. Evaluation of the Plio-Pleistocene astronomical timescale. *Paleoceanography* 11,
827 391–413.

828 Mader, D., Cleaveland, L., Bice, D., Montanari, A., Koeberl, C., 2004. High-resolution
829 cyclostratigraphic analysis of multiple climate proxies from a short Langhian pelagic succession
830 in the Conero Riviera, Ancona (Italy). *Palaeogeography Palaeoclimatology Palaeoecology* 211,
831 325–344.

832 Miller, K.G., Wright, J.D., Fairbanks, R.G., 1991. Unlocking the ice house: Oligocene–Miocene
833 oxygen isotopes, eustasy and margin erosion. *Journal of Geophysical Research* 96, 6829–
834 6848.

835 Miller, K.G., Kominz, M.A., Browning, J.V., Wright, J.D., Mountain, G.S., Katz, M.E., Sugarman,
836 P.J., Cramer, B.S., Christie-Blick, N., Pekar, S.F., 2005. The Phanerozoic record of global sea-
837 level change. *Science* 310, 1293–1298.

838 Montanari, A., Beaudoin, B., Chan, L.S., Coccioni, R., Deino, A., De Paolo, D.J., Emmanuel, L.,
839 Fornaciari, E., Krüger, M., Lundblad, S., Mozzato, C., Portier, E., Renard, M., Rio, D., Sandroni,
840 P., Stankiewicz, A., 1997. Integrated stratigraphy of the Middle and Upper Miocene pelagic
841 sequence of the Conero Riviera (Marche region, Italy). In: Montanari, A., Odin, G.S., Coccioni,
842 R. (Eds.), *Miocene Stratigraphy: An Integrated Approach*. *Developments in Palaeontology and*
843 *Stratigraphy* 15., Elsevier, Amsterdam, p. 409–450.

844 Morandi, N., Tateo, F., 1992. Mineralogy of pelitic "Bisciaro" & "Schlier" sediments in S. Croce and
845 Moria sections (Marche region, Italy). *Mineralogica Petrographica Acta* 35, 235–255.

846 Morrow, E., Mitrovica, J., Forte, A., Glišović, P., Huybers, P., 2012. An enigma in estimates of the
847 Earth's dynamic ellipticity. *Geophysical Journal International* 191, 1129–1134,
848 doi:10.1111/j.1365-246X.2012.05703.x.

849 Mourik, A.A., Bijkerk, J.F., Cascella, A., Hüsing, S.K., Hilgen, F.J., Lourens, L.J., Turco, E., 2010.
850 Astronomical tuning of the La Vedova high cliff section (Ancona, Italy) - implications of the
851 Middle Miocene climate transition for Mediterranean sapropel formation. *Earth and Planetary*
852 *Science Letters* 297, 249–261.

853 Nijenhuis, I.A., Schenau, S.J., Van der Weijden, C.H., Hilgen, F.J., Lourens, L.J., Zachariasse, W.J.,
854 1996. On the origin of upper Miocene sapropelites: A case study from the Faneromeni section,
855 Crete (Greece). *Paleoceanography* 11, 633–645.

856 Paillard, D., Labeyrie, L., Yiou, P., 1996. Macintosh program performs time-series analysis. *Eos* 77,
857 379.

858 Poulton, S.W., Raiswell, R., 2002. The low-temperature geochemical cycle of iron: from continental
859 fluxes to marine sediment deposition. *American Journal of Science* 302, 774–805.

860 Ragueneau, O., Tréguer, P., Leynaert, A., Anderson, R.F., Brzezinski, M.A., DeMaster, D.J.,
861 Dugdale, R.C., Dymond, J., Fischer, G., François, R., Heinze, C., Maier-Reimer, E., Martin-
862 Jézéquel, V., Nelson, D.M., Quéguiner, B., 2000. A review of the Si cycle in the modern ocean:
863 Recent progress and missing gaps in the application of biogenic opal as a paleoproductivity
864 proxy. *Global and Planetary Change* 26, 317–365.

865 Ricci Lucchi, F., Ori, G.G., 1985. Field excursion D: syn-orogenic deposits of a migrating basin
866 system in the NW Adriatic Foreland. In Allen, P.H., Homewood, P., Williams, G. (Eds.),
867 Excursion guidebook. Foreland Basins Symposium, Fribourg, p. 137–176.

868 Rögl, F., 1998. Palaeogeographic considerations for Mediterranean and Paratethys Seaways
869 (Oligocene to Miocene). - *Annalen des Naturhistorischen Museums in Wien* 99A: 279–310.

870 Sandroni, P., 1985. Rilevamento geologico al 1: 10.000 e litostratigrafia di alcune sezioni dello
871 Schlier nel bacino marchigiano esterno e studio mineralogico e petrografico di una sezione
872 ricostruita nell'anticlinale del Conero. Unpubl. PhD Thesis, University of Urbino, 188 pp.

873 Schenau, S.J., Antonarakou, A., Hilgen, F.J., Lourens, L.J., Nijenhuis, I.A., van der Weijden, C.H.,
874 Zachariasse, W.J., 1999. Organic-rich layers in the Metochia section (Gavdos, Greece):
875 evidence for a single mechanism of sapropel formation during the past 10 My. *Marine Geology*
876 153, 117–135.

877 Sprovieri, R., 1992. Mediterranean Pliocene biochronology: An high resolution record based on
878 quantitative planktonic foraminifera distribution. *Rivista Italiana di Paleontologia e Stratigrafia*
879 98, 61–100.

880 Sprovieri, M., Caruso, A., Foresi, L. M., Bellanca, A., Neri, R., Mazzola, S., Sprovieri, R., 2002.
881 Astronomical calibration of the upper Langhian/lower Serravallian record of Ras il-Pellegrin
882 section (Malta island, central Mediterranean). *Rivista Italiana di Paleontologia e Stratigrafia*
883 108, 183–193.

884 Sprovieri, R., Sprovieri, M., Caruso, A., Pelosi, N., Bonomo, S., Ferraro, L., 2006. Astronomic
885 forcing on the planktonic foraminifera assemblage in the Piacenzian Punta Piccola section
886 (southern Italy). *Paleoceanography* 21, doi:10.1029/2006PA001268.

887 Tian, J., Yang, M., Lyle, M.W., Wilkens, R., Shackford, J.K., 2013. Obliquity and long eccentricity
888 pacing of the Middle Miocene climate transition. *Geochemistry Geophysics Geosystems* 14,
889 1740–1755.

890 Torrence, C., Compo, G.P., 1998. A practical guide to wavelet analysis. *Bulletin of American*
891 *Meteorological Society* 79, 61–78.

892 Turco, E., Cascella, A., Gennari, R., Hilgen, F.J., Iaccarino, S.M., Sagnotti, L., 2011a. Integrated
893 stratigraphy of the La Vedova section (Conero Riviera, Italy) and implications for the
894 Burdigalian/Langhian boundary. *Stratigraphy* 8, 89–110.

895 Turco, E., Iaccarino, S. M., Foresi, L., Salvatorini, G. Riforgiato, F., Verducci, M., 2011b. Revisiting
896 the taxonomy of the intermediate stages in the *Globigerinoides* – *Praeorbulina* lineage.
897 *Stratigraphy* 8, 163-187.

898 Van Couvering, J.A., Castradori, D., Cita, M.B., Hilgen, F.J., Rio, D., 2000. The base of the
899 Zanclean Stage and of the Pliocene Series. *Episodes* 23, 179–187.

900 Van Os, B.J.H., Lourens, H.J., Hilgen, F.J., De Lange, G.J., Beaufort, L., 1994. The formation of
901 Pliocene sapropels and carbonate cycles in the Mediterranean: Diagenesis, dilution, and
902 productivity. *Paleoceanography* 9, 601–617.

903 Vincent, E., Berger, W.H., 1985. Carbon dioxide and polar cooling in the Miocene: the Monterey
904 hypothesis. In Broecker, W.S., Sundquist, E.T. (Eds.), *The Carbon Cycle and Atmospheric*
905 *CO₂: Natural Variations Archean to Present*. Geophysical Monograph Series, vol. 32. AGU,
906 Washington, DC, p. 455–468.

907 Wehausen, R., Brumsack, H.-J., 2000. Chemical cycles in Pliocene sapropel-bearing and sapropel-
908 barren eastern Mediterranean sediments. *Palaeogeography Palaeoclimatology Palaeoecology*
909 158, 325–352.

910 Woodruff, F., Savin, S., 1991. Mid-Miocene isotope stratigraphy in the deep sea: high resolution
911 correlations, paleoclimatic cycles, and sediment preservation. *Paleoceanography* 6, 755–806.

912 Zeeden, C., Hilgen, F.J., Hüsing, S.K., Lourens, L.J. 2014. The Miocene astronomical time scale 9-
913 12 Ma: New constraints on tidal dissipation and their implications for paleoclimatic
914 investigations. *Paleoceanography*.29, 296–307.

915 Ziegler, M., Tuenter, E., Lourens, L.J., 2010. The precession phase of the boreal summer monsoon
916 as viewed from the eastern Mediterranean (ODP Site 968). *Quaternary Science Reviews* 29,
917 1481–1490.

918 Zhisheng, A., Kutzbach, J.E., Prell, W.L., Porter, S.C., 2001. Evolution of Asian monsoons and
919 phased uplift of the Himalaya-Tibetan plateau since Late Miocene times. *Nature* 411, 62-66.

920

921 **Figure captions**

922

923 Figure 1. Location map for the Lower La Vedova Beach section.

924

925 Figure 2. Photographs of the Lower La Vedova Beach section showing: a) the upper part from
926 Megabed IX to the top; b and c) the lower part from the base (Megabed II) to Megabed VIII. The
927 improvement in the quality of the exposure between summer 2009 (b) and summer 2012 (c) led to
928 the determination of the fault offset and to the revised correlation of megabeds (see also text and
929 Supplementary material A).

930

931 Figure 3. The revised composite lithological column and the color record of the Lower La Vedova
932 Beach section with the magnetostratigraphy and the distribution pattern of the calcareous plankton
933 marker species. The gray band indicates the missing interval in the composite section of Turco et
934 al. (2011a). The stratigraphic position of calcareous plankton events is shown beside the
935 distribution patterns; numbers 1, 2 and 3 indicate the First Occurrences (FOs) of *Globigerinoides*
936 *sicanus* (3 apertures), *Praeorbulina glomerosa curva* and *P. glomerosa glomerosa*, respectively.
937 The magnetobiostratigraphic record is correlated to ATNTS2004/2012 and the Mediterranean
938 biozonations of Iaccarino and Salvatorini (1982) and Iaccarino (1985) for planktonic foraminifera
939 and of Fornaciari et al. (1996) for calcareous nannofossils, both emended in Di Stefano et al.
940 (2008). The planktonic foraminifer MMi3/MMi4 zonal boundary, identified by the FO of
941 *Globigerinoides sicanus* (3 apertures) in the Mediterranean, was emended in Iaccarino et al.
942 (2011).

943

944 Figure 4. The MS and the most relevant elemental (Al, CaCO₃, CA/Al, Rb/Sr, Si/Al, Rb/Al and Ti/Al)
945 records and their 3 and 5 point moving average curves of the Lower La Vedova Beach section.

946

947 Figure 5. Wavelet spectra of the MS, Al, CA/Al and Rb/Sr records of the Lower La Vedova Beach
948 section in the depth domain. Wavelet analysis was carried out using the Torrence and Compo
949 (Torrence and Compo, 1998) method implemented in MATLAB. The autocorrelation coefficient of
950 individual datasets and a Morlet wavelet was used.

951

952 Figure 6. Blackman-Tukey spectra of the MS, Al, Ca/Al and Rb/Sr records for the 0-40 m interval in
953 the Lower La Vedova Beach section in the depth domain and results of bandpass filtering of the
954 prominent ~ 7 m cyclicity. The Analyseries program of Paillard et al. (1996) and an 80% confidence
955 level were used. The 80% confidence level interval is indicated by the lower and upper spectra (red
956 and green lines, respectively).

957

958 Figure 7. Blackman-Tukey spectra of the MS, Al, Ca/Al and Rb/Sr records for the 40-63m interval
959 in the Lower La Vedova Beach section in the depth domain and results of bandpass filtering of the
960 prominent ~ 3 -3.5m cyclicity at frequencies of 0.30 ± 0.20 , 0.36 ± 0.084 , 0.35 ± 0.15 and $0.28 \pm$
961 0.12 cycle/m, respectively. The Analyseries program of Paillard et al. (1996) and 80% confidence
962 level were used. The 80% confidence level interval is indicated by the lower and upper spectra (red
963 and green lines, respectively).

964

965 Figure 8. Bandpass filtering of the higher frequency spectral peaks at frequencies of 0.65 ± 0.35
966 (Ca/Al), 0.70 ± 0.65 (CaCO₃) and 0.73 ± 0.14 (Rb/Al) cycle/m, corresponding to ~ 1.5 m in the 0-
967 40m interval, and at frequencies of 1.35 ± 0.85 (Ca/Al), 1.37 ± 0.85 (CaCO₃) and 1.50 ± 0.32
968 (Rb/Al) cycle/m, corresponding to ~ 0.7 m in the 40-63m interval.

969

970 Figure 9. Tuning of the Lower La Vedova Beach section to the Laskar 2004 (1,1) eccentricity target
971 curves. The middle points of megabeds and the intervening marl intervals have been correlated to
972 minima and maxima of 100 kyr eccentricity, respectively. The phase relation is inferred from *G.*
973 *trilobus* gr., MS and Rb/Sr records.

974

975 Figure 10. MTM spectra of the eccentricity tuned Rb/Sr and MS time series and comparison of the
976 extracted ~ 100 -kyr cycle with eccentricity.

977

978 Figure 11. MTM spectra of the eccentricity tuned Rb/Sr and Rb/Al time series and bandpass filtered
979 precession-related components shown as overlay on these time series.

980

981 Figure 12. Tuning of the MS, Rb/Sr, Rb/Al, Ti/Al and Ca/Al 3 pma records of the Lower La Vedova
982 Beach section to the Laskar 2004_(1,1) 65N lat summer insolation. The tie-points used for the tuning
983 are indicated by crosses.

984 **Table captions**

985

986 Table 1. Comparison between the revised stratigraphic position of the magnetic reversals and
987 average sedimentation rates in the Lower La Vedova Beach section (this paper) and those of Turco
988 et al. (2011a). Comparison between the revised stratigraphic position, magnetostratigraphic
989 position and calibration of the calcareous plankton events in the Lower La Vedova Beach section
990 (this paper) and those of Turco et al. (2011a). Δ indicates the age difference of bioevents between
991 Turco et al. (2011a) and the present paper. Magnetostratigraphic position and calibration of the
992 calcareous plankton events in the Lower La Vedova Beach section are compared with those at
993 DSDP Site 372 (Balearic Basin).

994

995 Table 2. Average values in olive gray and in greenish gray layers and the t values resulting from an
996 independent Student t Test performed on selected planktonic foraminifer taxa and elemental ratios.
997 The difference of the means of a proxy with respect to the two types of sediment color is
998 statistically significant when $t_{(0.975)}$ value is >1.96 for $n= 239$ samples (planktonic foraminifera) and
999 $n= 566$ samples (elemental ratios).

1000

1001 Table 3. Astronomical ages of magnetic reversal boundaries and calcareous plankton events
1002 according to the tuning to eccentricity and insolation. It is also indicated the age difference of
1003 magnetic reversals between ATNTS2004/2012 and the astronomical calibration to eccentricity at La
1004 Vedova ($\Delta 1$) between ATNTS2004/2012 and the astronomical calibration to insolation at La Vedova
1005 ($\Delta 2$) and between the astronomical calibration to eccentricity and to insolation at La Vedova ($\Delta 3$).
1006 Astronomical calibration of calcareous plankton events is compared with the magnetostratigraphic
1007 age. It is indicated the age difference of the bioevents between magnetostratigraphic and
1008 astronomical calibration to eccentricity at La Vedova ($\Delta 1$), between magnetostratigraphic and
1009 astronomical calibration to insolation ($\Delta 2$) and between astronomical calibration to eccentricity and
1010 to insolation ($\Delta 3$). Astronomical ages are calculated by means of linear interpolation between the
1011 two nearest calibration points, which are the tuned tie-points of proxy records (Fig. 12), assuming
1012 constant sedimentation rates.

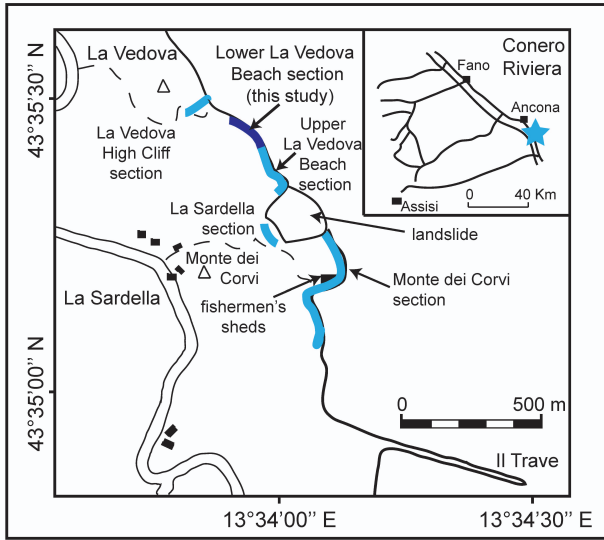


Figure 1



Figure 2

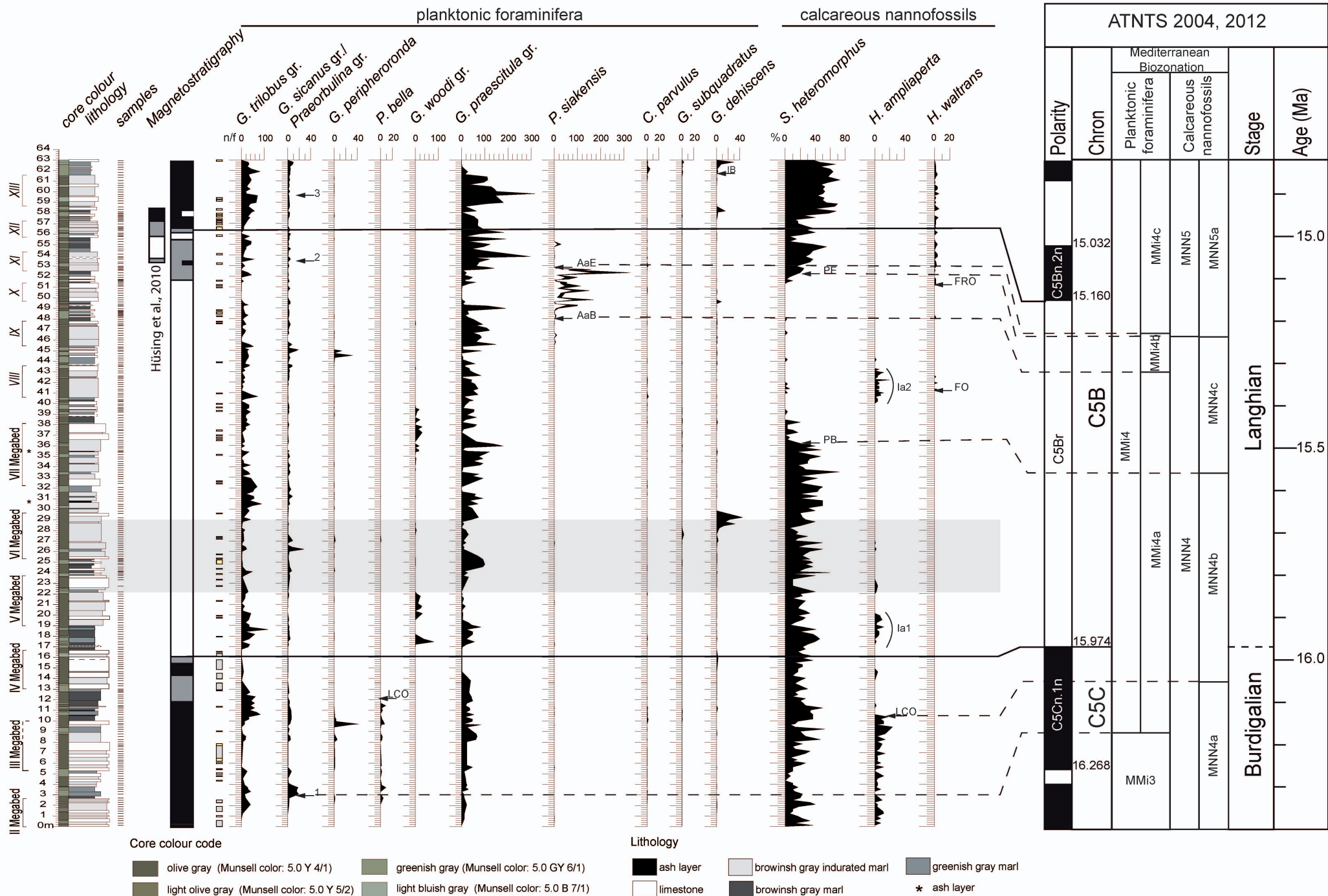


Figure 3

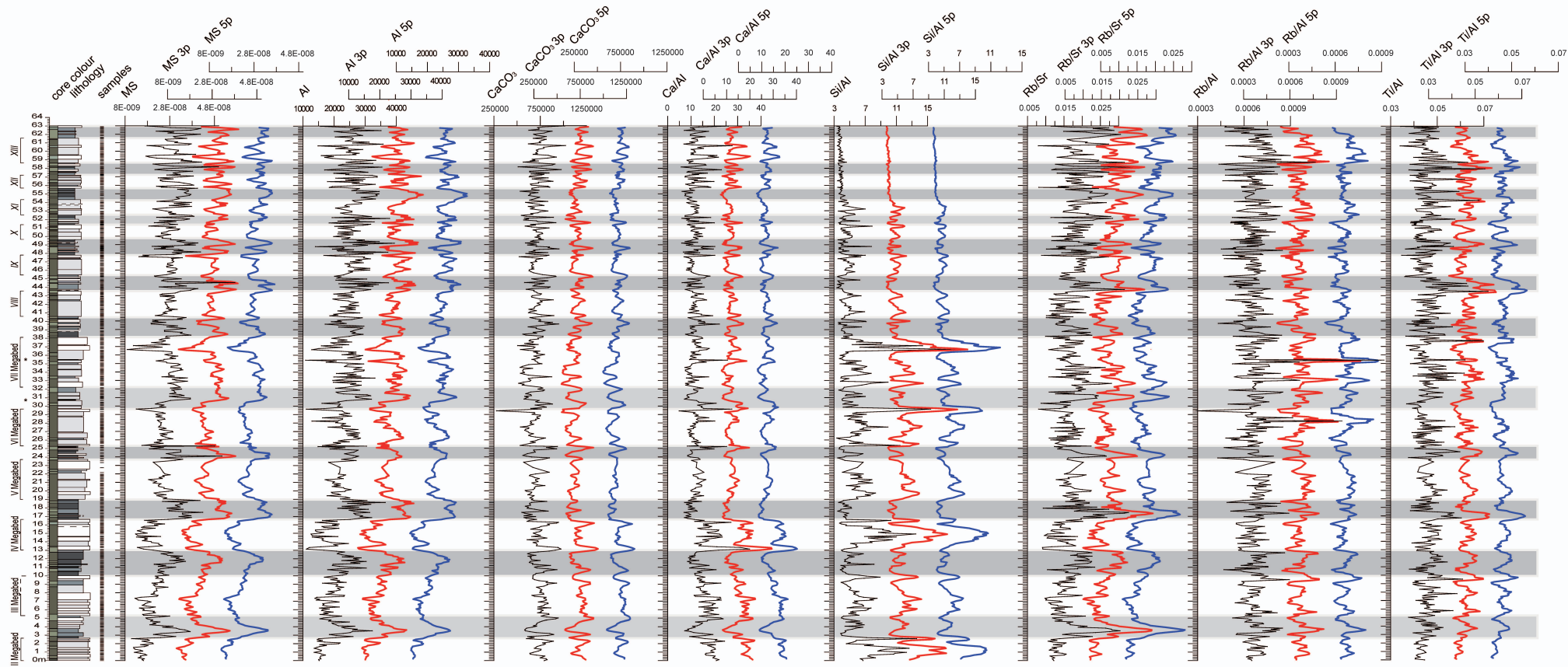


Figure 4

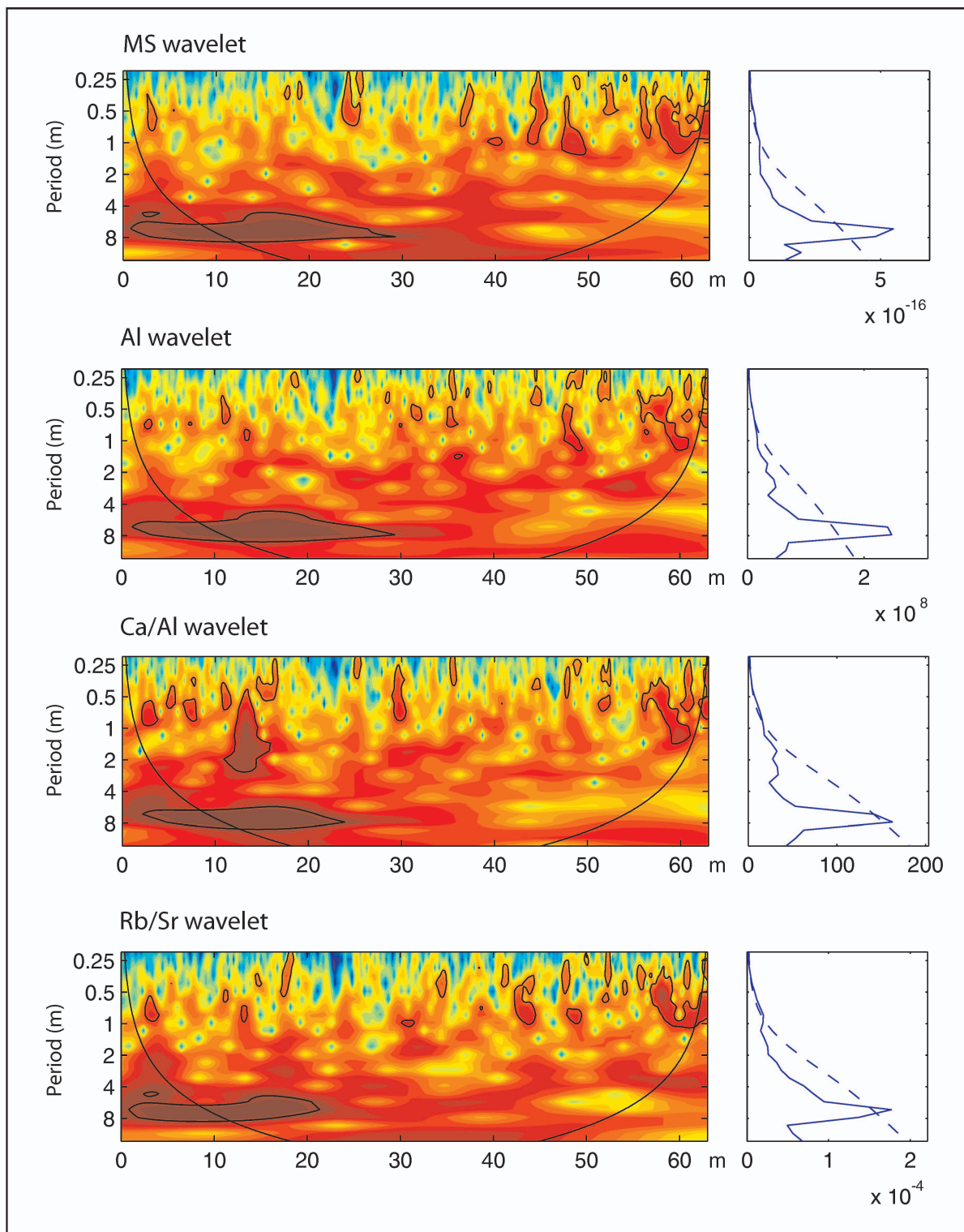


Figure 5

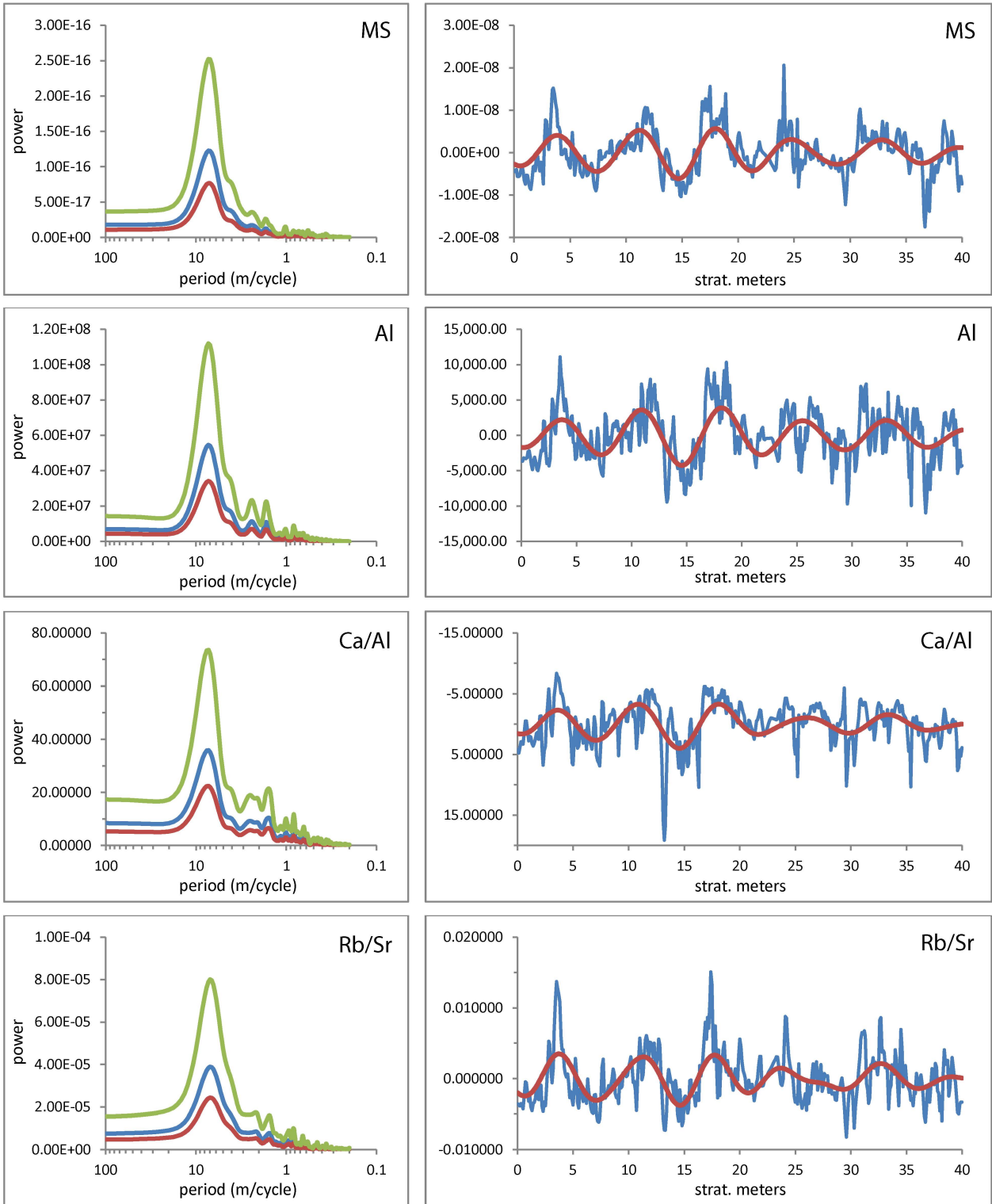


Figure 6

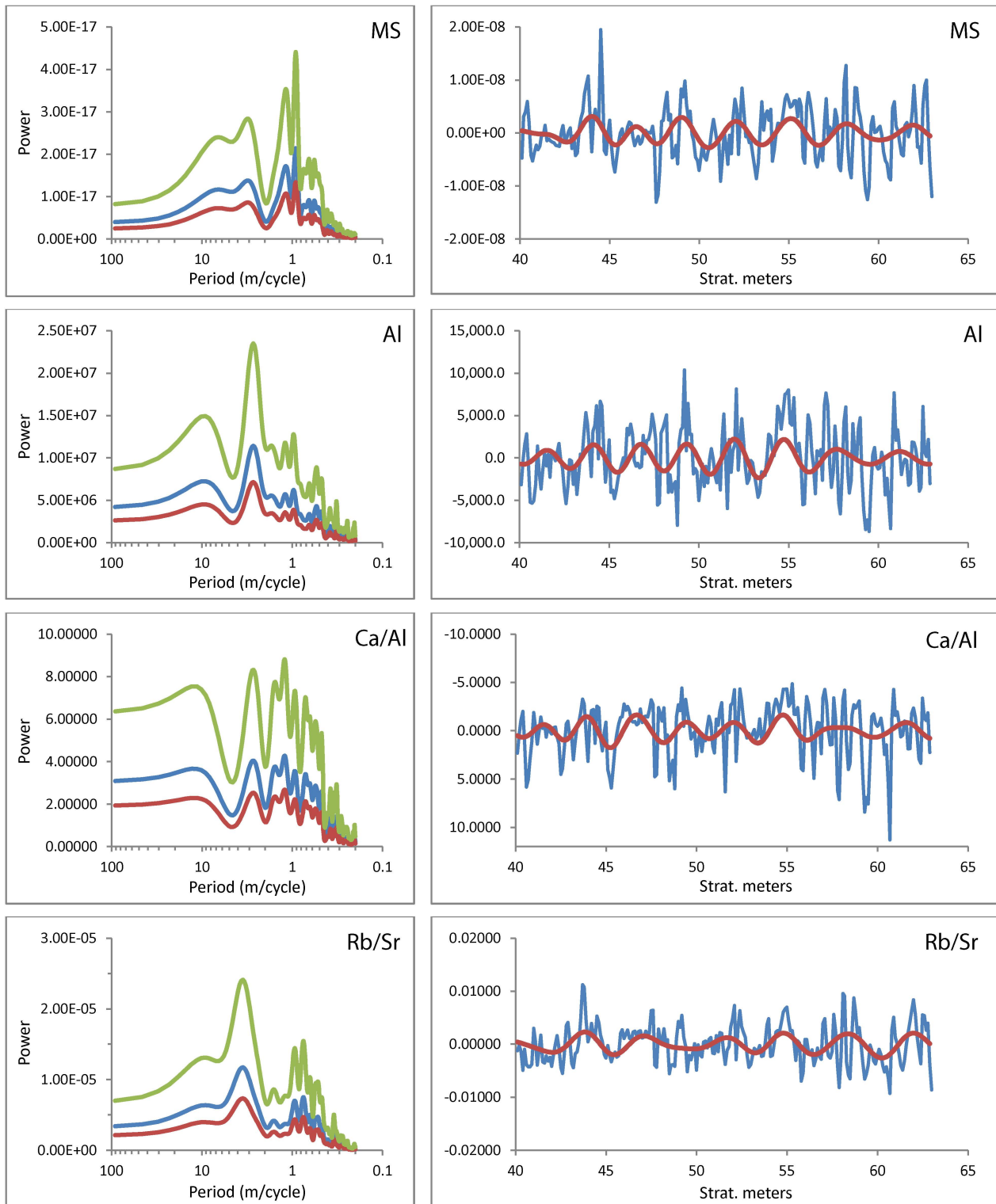


Figure 7

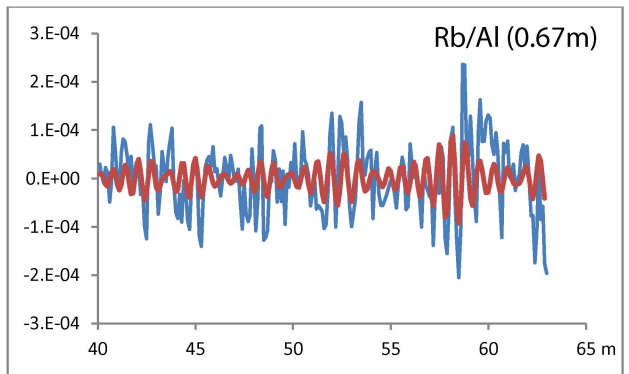
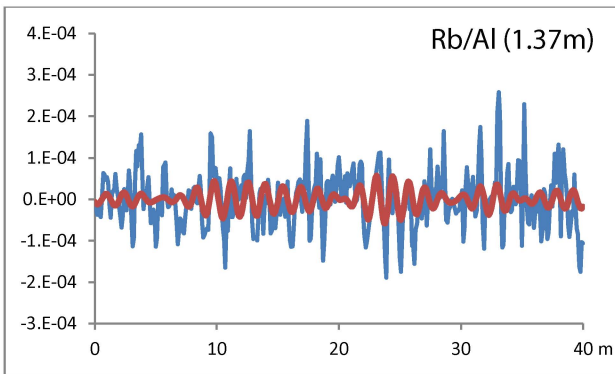
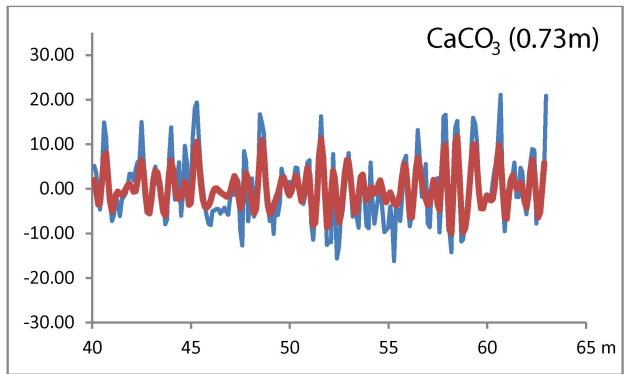
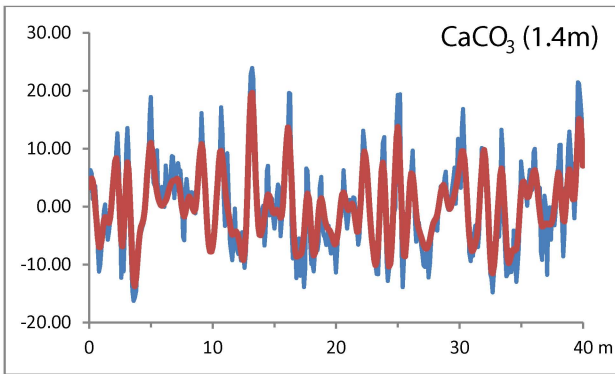
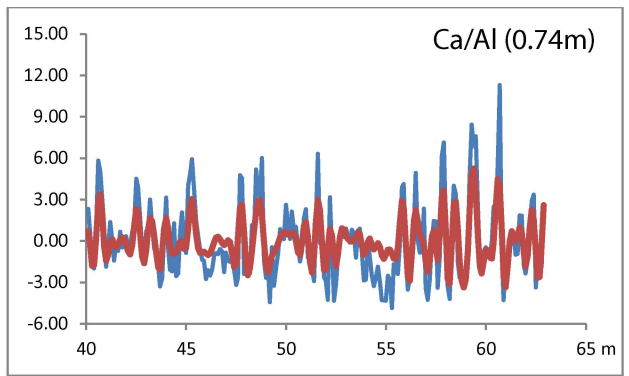
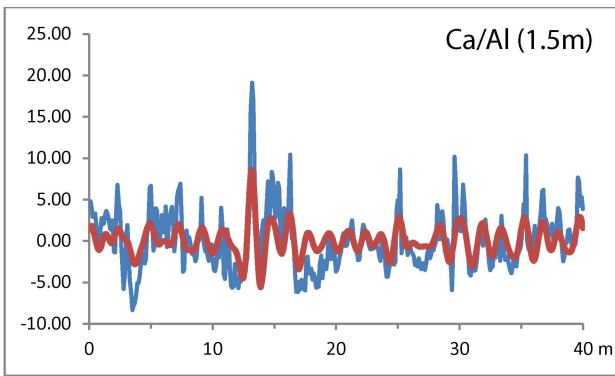


Figure 8

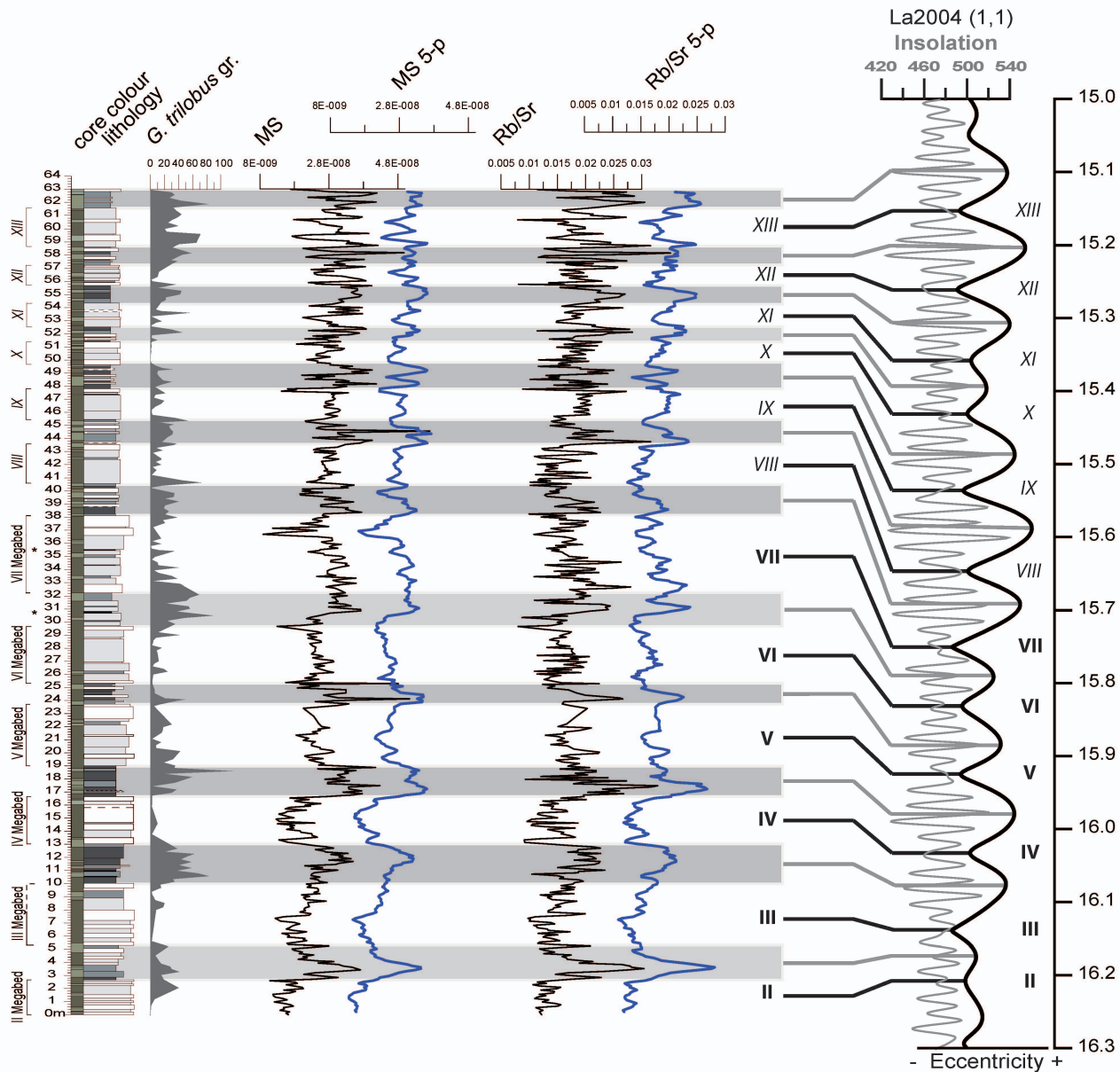


Figure 9

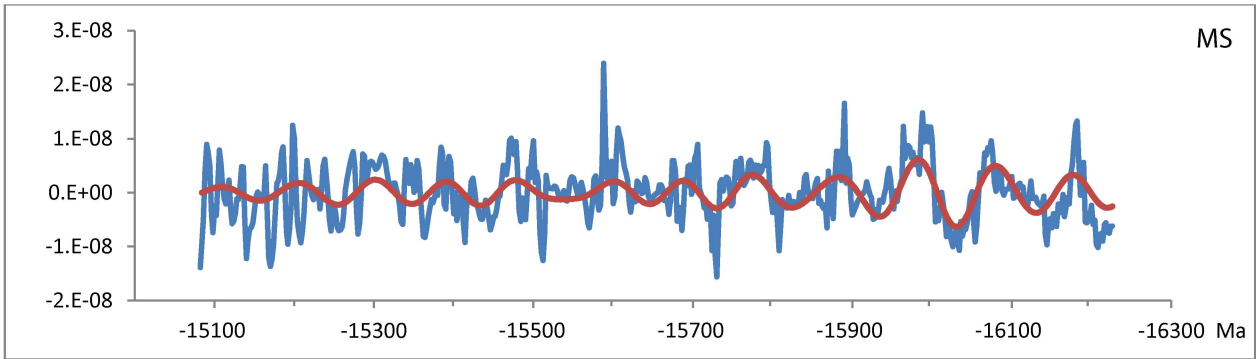
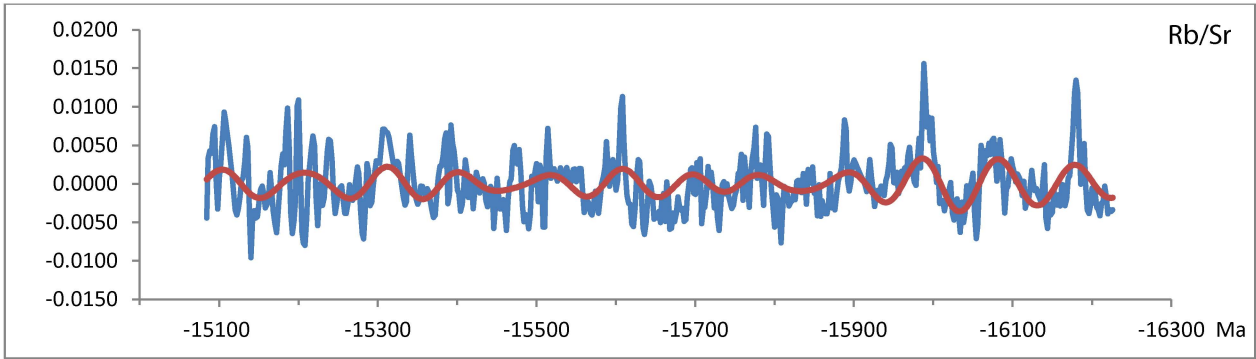
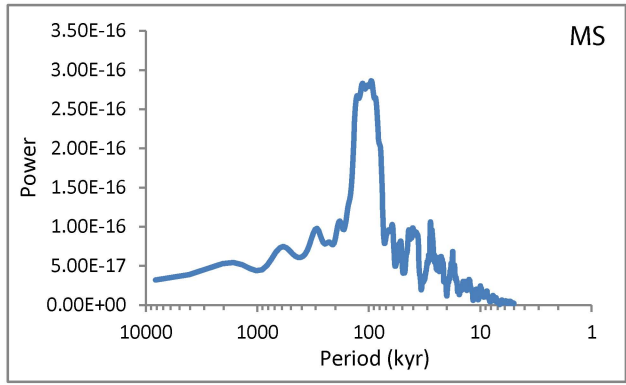
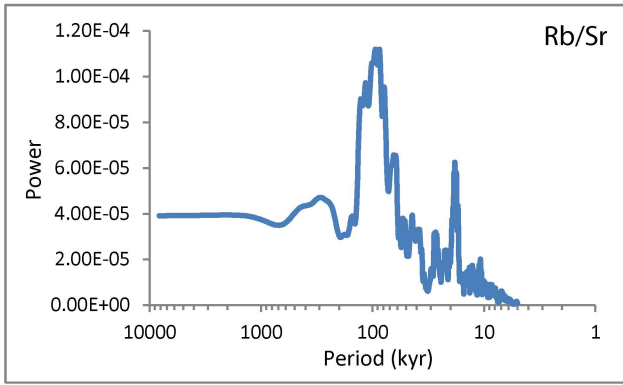


Figure 10

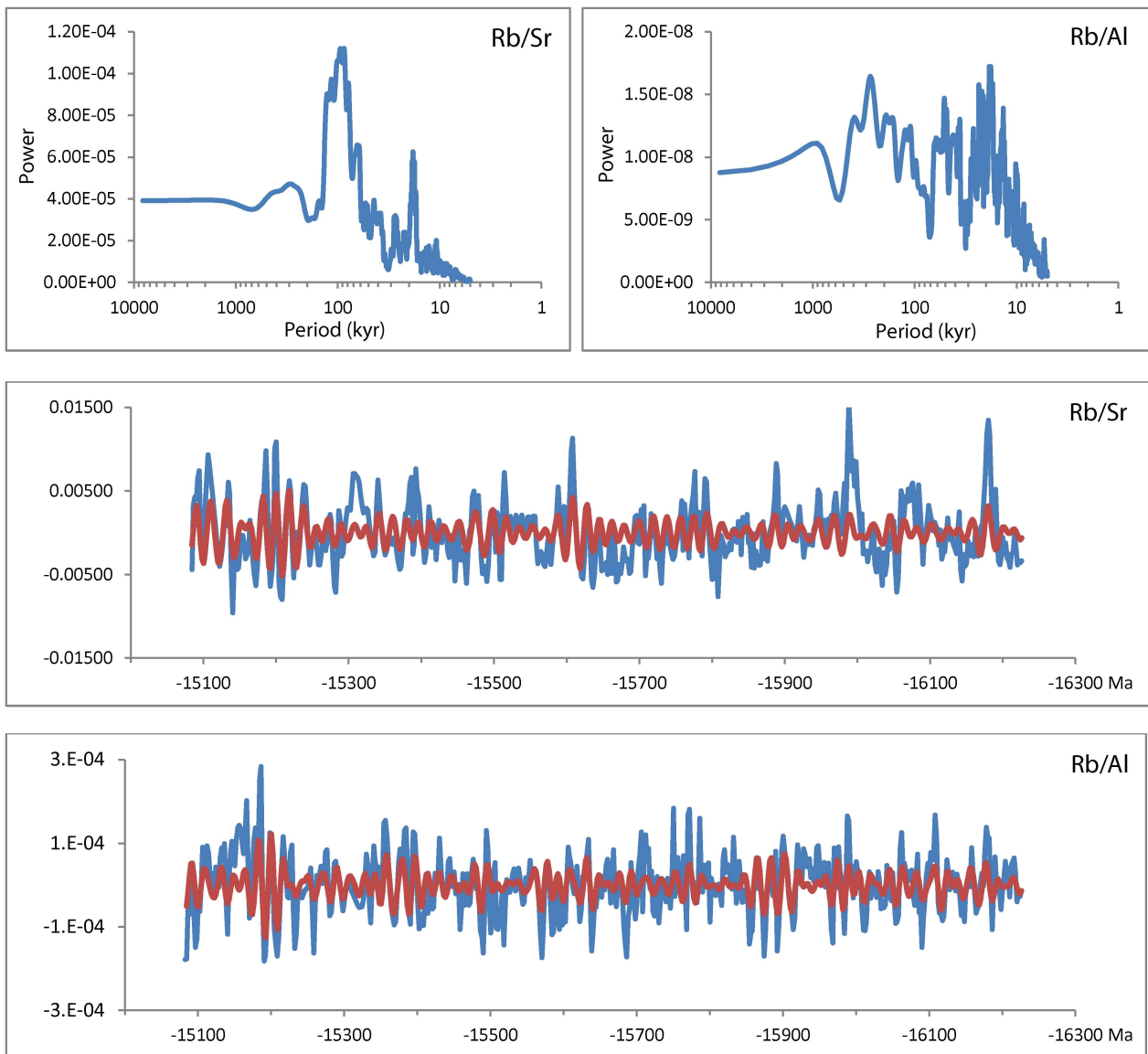


Figure 11

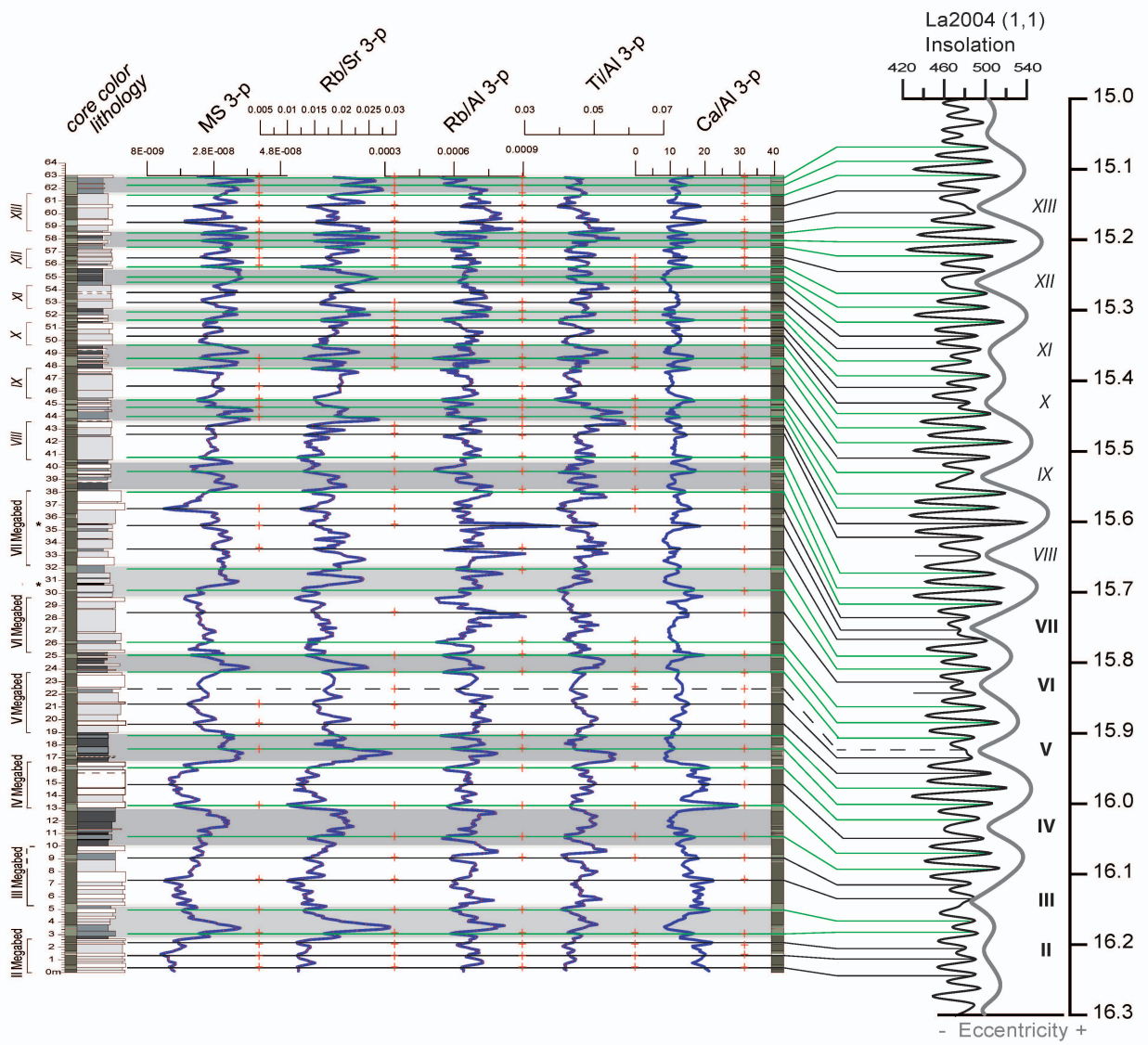


Figure 12

Lower La Vedova Beach section									
Magnetic reversal boundaries		hypothesis b_ Turco et al. 2011			hypothesis b_ This paper				
	ATNTS 2012 (Ma)	Strat. interval (m)	Mean strat. position (m)	Average sed. rate (cm/kyr)	Strat. interval (m)	Mean strat. position (m)	Average sed. rate (cm/kyr)		
C5Bn.2n (y)	15.032	57.16 _ 57.58	57.370 ± 0.210	C5Bn.2n: 6.035 ± 0.363	63.95 _ 64.37	64.160 ± 0.210		C5Bn.2n: 6,074	± 0.402
C5Bn.2n (o)	15.160	49.39 _ 49.90	49.645 ± 0.255	C5Br: 4.165 ± 0.063	56.08 _ 56.69	56.385 ± 0.305		C5Br: 4.986	± 0.075
C5Cn.1n (y)	15.974	15.49 _ 16.00	15.745 ± 0.255	C5Cn.1n: 6.342 ± 1.073	15.49 _ 16.10	15.795 ± 0.305		C5Cn.1n: 6,359	± 1.090
C5Cn.1n (o)	16.268	-5.80 _ 0.00	-2.900 ± 2.900		-5.80 _ 0.00	-2.900 ± 2.900			
Lower La Vedova Beach section								DSDP Site 372	
Bioevent	hypothesis b_ Turco et al. 2011		hypothesis b_ This paper		Δ	(sub)chron	(Abdul Aziz et al. 2008, Di Stefano et al. 2008)		
	Mean strat. position (m)	Magnetostrat. Age (Ma)	Mean strat. position (m)	Magnetostrat. Age (Ma)	Age (Ma)		(sub)chron	Age (Ma)	
<i>G. dehiscens</i> IB	54.970 ± 0.130	15.072 ± 0.002	61.760 ± 0.130	15.072 ± 0.002	0.000	C5Bn.2n	C5Bn.2n	-	
<i>P. gl. glomerosa</i> FO	52.925 ± 0.085	15.106 ± 0.001	59.715 ± 0.085	15.105 ± 0.001	0.000	C5Bn.2n	C5Bn.2n	15.102	
<i>P. glomerosa curva</i> FO	46.685 ± 0.135	15.231 ± 0.003	53.475 ± 0.135	15.218 ± 0.002	-0.013	C5Br	-	-	
<i>P. siakensis</i> A _a E	46.065 ± 0.105	15.246 ± 0.003	52.805 ± 0.055	15.232 ± 0.001	-0.014	C5Br	C5Br	15.435	
<i>S. heteromorphus</i> PE	45.430 ± 0.110	15.261 ± 0.003	52.220 ± 0.110	15.244 ± 0.002	-0.018	C5Br	C5Br	15.527	
<i>H. waltrans</i> FRO	44.395 ± 0.115	15.286 ± 0.003	51.185 ± 0.115	15.264 ± 0.002	-0.022	C5Br	C5Br	15.476	
<i>P. siakensis</i> A _a B	41.255 ± 0.095	15.361 ± 0.002	48.045 ± 0.095	15.327 ± 0.002	-0.034	C5Br	-	-	
<i>H. ampliaperta</i> la ₂ E	36.220 ± 0.090	15.482 ± 0.002	43.010 ± 0.090	15.428 ± 0.001	-0.054	C5Br	-	-	
<i>H. ampliaperta</i> AS	-	-	-	-	-	-	C5Br	15.899	
<i>H. ampliaperta</i> la ₂ B	33.305 ± 0.105	15.552 ± 0.003	40.095 ± 0.105	15.487 ± 0.002	-0.066	C5Br	-	-	
<i>S. heteromorphus</i> PB	29.480 ± 0.100	15.644 ± 0.002	36.270 ± 0.100	15.563 ± 0.002	-0.081	C5Br	C5Br	15.949	
<i>P. bella</i> LCO	12.205 ± 0.095	16.030 ± 0.001	12.205 ± 0.095	16.030 ± 0.002	0.001	C5Cn.1n	-	-	
<i>H. ampliaperta</i> LCO	10.490 ± 0.110	16.057 ± 0.002	10.490 ± 0.110	16.057 ± 0.002	0.001	C5Cn.1n	-	-	
<i>G. sicanus</i> (3ap.) FO?	2.895 ± 0.185	16.177 ± 0.003	2.895 ± 0.185	16.177 ± 0.003	0.000	C5Cn.1n	-	-	

Table 1

Independent Student t Test

	olive gray	greenish gray	t _(0,975) value
<i>Globigerinoides trilobus</i> gr.	19.0302	30.5636	3.8476
<i>Globigerinoides sicanus</i> / <i>Praeorbulina</i> gr.	1.9064	4.8687	4.5096
Ca/Al	12.6132	14.3637	3.8996
Ti/Al	0.0476	0.0455	-2.2483
Zr/Al	0.0014	0.0012	-4.5502
V/Al	0.0067	0.0060	-1.5367
Ba/Al	0.0219	0.0221	0.2436
Rb/Al	0.0007	0.0006	-8.3759
Rb/Sr	0.0175	0.0176	0.3573

Table 2

Magnetic reversal boundaries	Stratigraphic position (m)	ATNTS 2012 (Ma)	Astronomical calibration eccentricity (Ma)	Astronomical calibration insolation (Ma)	$\Delta 1$ (Ma)	$\Delta 2$ (Ma)	$\Delta 3$ (Ma)
C5Bn.2n (o)	56.385 ± 0.305	15.160	15.264 ± 0.009	15.251 ± 0.013	-0.104	-0.091	0.013
C5Cn.1n (y)	15.795 ± 0.305	15.974	16.017 ± 0.005	16.030 ± 0.006	-0.043	-0.056	-0.012

Bioevents	Mean strat. position (m)	(sub)chron	Magnetostratigraphic calibration (Ma)	Astronomical calibration Eccentricity (Ma)	Astronomical calibration Insolation (Ma)	$\Delta 1$ (Ma)	$\Delta 2$ (Ma)	$\Delta 3$ (Ma)
<i>G. dehiscens</i> IB	61.760 ± 0.130	C5Bn.2n	15.072 ± 0.002	15.113 ± 0.003	15.101 ± 0.003	-0.041	-0.030	0.011
<i>P. gl. glomerosa</i> FO	59.715 ± 0.085	C5Bn.2n	15.105 ± 0.001	15.163 ± 0.002	15.153 ± 0.002	-0.057	-0.048	0.010
<i>P. glomerosa curva</i> FO	53.475 ± 0.135	C5Br	15.218 ± 0.002	15.356 ± 0.004	15.343 ± 0.004	-0.137	-0.125	0.013
<i>P. siakensis</i> A ₃ E	52.805 ± 0.055	C5Br	15.232 ± 0.001	15.374 ± 0.001	15.359 ± 0.001	-0.142	-0.128	0.014
<i>S. heteromorphus</i> PE	52.220 ± 0.110	C5Br	15.244 ± 0.002	15.389 ± 0.003	15.372 ± 0.004	-0.145	-0.128	0.017
<i>H. waltrans</i> FRO	51.185 ± 0.115	C5Br	15.264 ± 0.002	15.414 ± 0.003	15.403 ± 0.003	-0.150	-0.138	0.012
<i>P. siakensis</i> A ₃ B	48.045 ± 0.095	C5Br	15.327 ± 0.002	15.502 ± 0.002	15.480 ± 0.002	-0.175	-0.153	0.022
<i>H. ampliapertura</i> la ₂ E	43.010 ± 0.090	C5Br	15.428 ± 0.001	15.625 ± 0.002	15.608 ± 0.003	-0.197	-0.180	0.018
<i>H. ampliapertura</i> la ₂ B	40.095 ± 0.105	C5Br	15.487 ± 0.002	15.680 ± 0.002	15.687 ± 0.002	-0.193	-0.200	-0.007
<i>S. heteromorphus</i> PB	36.270 ± 0.100	C5Br	15.563 ± 0.002	15.736 ± 0.001	15.742 ± 0.001	-0.172	-0.178	-0.006
<i>P. bella</i> LCO	12.205 ± 0.095	C5Cn.1n	16.030 ± 0.002	16.067 ± 0.001	16.078 ± 0.001	-0.037	-0.048	-0.011
<i>H. ampliapertura</i> LCO	10.490 ± 0.110	C5Cn.1n	16.057 ± 0.002	16.093 ± 0.002	16.094 ± 0.001	-0.036	-0.036	-0.001
<i>G. sicanus</i> (3ap.) FO?	2.895 ± 0.185	C5Cn.1n	16.177 ± 0.003	16.189 ± 0.002	16.189 ± 0.005	-0.012	-0.012	0.000

Table 3